We turned a hard-to-reuse binary-star method into agent-callable tools, then used it to find 41,466 candidates.

Draft version August 12, 2026
Typeset using LaTeX **twocolumn** style in AASTeX631

arXiv:2608.10866v1 [astro-ph.SR] 11 Aug 2026

Spectroscopic Binary Detection as Agent-Callable Tools: Detecting 40,000+ Main-Sequence Binary Candidates from SDSS DR19 APOGEE Spectra

Serat M. Saad[1] and Yuan-Sen Ting[1,2,3]

[1]*Department of Astronomy, The Ohio State University, 140 West 18th Avenue, Columbus, OH 43210, USA*
[2]*Center for Cosmology and AstroParticle Physics (CCAPP), The Ohio State University, Columbus, OH 43210, USA*
[3]*Max-Planck-Institut für Astronomie, Königstuhl 17, D-69117 Heidelberg, Germany*

ABSTRACT

Unresolved binaries are common in spectroscopic surveys, and their blended light biases the parameters inferred for them. Methods to detect them exist, but applying one to a new data release is limited mostly by operating know-how that is rarely written down. We package the double-lined spectroscopic binary decomposition of El-Badry et al. (2018b) for reuse on APOGEE spectra, with the executable operations as nine tool servers built on the Model Context Protocol (MCP) and the operating decisions as a Skill. Run over the 238,205 DR19 dwarfs under a fixed driver script, the classifier flags 41,466 SB2 candidates with median mass ratio $q = 0.91$, about fifteen times the 2,645 identified in DR13, though not at matched purity. The 8.1% control false-positive rate implies that close to 40% are single stars, so we release the sample as a candidate list. Refitting the individual visits confirms 68.5% of the multiply-visited SB2 and adds 519 single-lined velocity variables and 8,981 orbit-ready systems. We compare the eccentricities of the best-sampled binaries and find no significant difference between the close twins ($q > 0.95$) and matched non-twins, which excludes an eccentricity excess of the kind measured at wide separations. An ablation of two operating decisions illustrates that a fresh agent recovers a removed decision only when its absence leaves a measurable trace in the fit. We release the tools, the Skill, and the DR19 catalog with its multi-epoch supplement.

Keywords: Spectroscopic binary stars, Close binary stars, Astronomy software, Astronomy data analysis, Sky surveys, Multiple stars



1. INTRODUCTION

Stars are commonly found not in isolation but as members of multiple systems. The multiplicity fraction depends on primary mass and on birth environment, from the near-unity companion frequency of O and B stars (Kobulnicky & Fryer 2007; Sana et al. 2012) through the ∼40–50% of solar-type field dwarfs (Raghavan et al. 2010; Kraus et al. 2011) to the cataloged hierarchies of the solar neighborhood (Tokovinin 2018). The distributions of mass ratio, period, and eccentricity that go with it are a basic input to stellar astrophysics, recording the fragmentation and dynamical processes of star-forming gas (Duchêne & Kraus 2013; Moe & Di Stefano 2017; Offner et al. 2023; Kroupa 1995; Tokovinin & Moe 2020; Offner et al. 2023) and the evolution of the stars (Izzard, Hawthorn & Gerhard 2016). A multi-object spectroscopic survey (e.g. Steinmetz et al. 2006; Cui et al. 2012; de Jong et al. 2019; Jin et al. 2024; Recio-Blanco et al. 2023) therefore observes a substantial population of unresolved multiples, in which two or more stars fall within a single fiber and their light combines into one composite spectrum.

A candidate list, not a clean binary census: the control test implies substantial contamination.

The reusable ingredient is operating judgment: tools expose the calculations; the Skill records how to use them.

1.1. *Spectroscopic binaries and their detection*

Binaries can be identified in several ways. Astrometrically, an unresolved companion displaces the photocenter and raises the *Gaia* renormalized unit weight error (RUWE; Belokurov et al. 2020; Penoyre et al. 2022; Lindegren et al. 2021) and can be fit as an astrometric orbit (Halbwachs et al. 2023; Shahaf et al. 2023; Kervella et al. 2019), while wide, resolved pairs are selected directly from *Gaia* astrometry (El-Badry & Rix 2018; El-Badry et al. 2021); see El-Badry (2024) for a review of *Gaia*'s impact on binary-star science. Spectroscopically, radial-velocity variations across epochs give orbits (Zucker & Mazeh 1994; Pourbaix et al. 2004; Price-Whelan et al. 2017), an approach that has been used for the close-binary population of APOGEE (Mazzola et al. 2020; Kounkel et al. 2021; Daher et al. 2022). The present

Composite spectra reveal companions, but reproducing the method requires choices that papers and code usually leave implicit.

work concerns the third case, the spectral signature of two stars blended in a single exposure.

Unresolved multiplicity is both a science target and a source of systematic error. When a single-star model is fit to a composite spectrum, the inferred effective temperature, surface gravity, and chemical abundances are biased, most of all at intermediate mass ratio where the secondary contributes enough flux to change the lines without producing a second set of lines (El-Badry et al. 2018a). Both data-driven (e.g. Ness et al. 2015; Ting et al. 2019) and physical (e.g. García Pérez et al. 2016) pipelines for deriving these stellar parameters inherit this bias equally, since both fit a single template to the data and have no way to represent a second component.

Recovering that second component from a single epoch is therefore both a correction to the stellar parameters and a measurement of the binary in its own right. Two families of method are used at survey scale. Cross-correlation approaches look for multiple peaks in the correlation of the observed spectrum against a template, and have been applied to Gaia-ESO (Merle et al. 2017) and to APOGEE (Kounkel et al. 2021). They target the double-lined spectroscopic binaries (SB2), in which the two sets of absorption lines are separated enough to appear as distinct peaks.

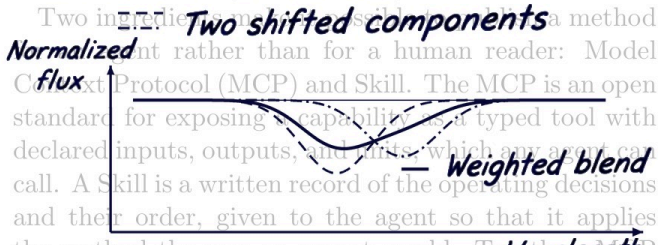
Forward modeling catches blended companions before two distinct correlation peaks become obvious.

Forward-modeling approaches instead build a two-component composite from a single-star spectral model, fit it to the observed spectrum, and compare the result to the best single-star fit. The decision rests on whether the second component improves the fit, not on whether it produces a countable second peak, so the classical SB2 is the large-separation limit of a wider class of composite spectra. El-Badry et al. (2018a) introduced the composite forward model and El-Badry et al. (2018b) built the DR13 SB2 catalog and the acceptance thresholds we adopt (hereafter EB18, and EB18a for the method paper). We adopt the forward-modeling decomposition of EB18 as our worked example, because it is fully specified, has a public implementation,[1] and has a published DR13 catalog to compare against.

1.2. *Publishing method know-how for agents*

A method like the EB18 decomposition is communicated as a paper and, increasingly, as public code. Neither one passes on the operating experience that makes the method run correctly on a new data set. The main choices are the normalization convention that cancels in the detection statistic, the pixels that must be masked, the signal-to-noise cap, the multi-start strategy for the mass ratio, the calibration of the acceptance thresholds, and the failure modes that give fake detections. These decisions are mostly tacit. They are spread across the source paper, the code, the calibration data, and the authors' judgment, and they are rarely written down as a procedure. A reader with the equations and the public code still has to work them out again, which is the step that limits the reuse of a published method.

Language models are beginning to change how such analyses are done. The capability rests on a line of work in machine learning: prompting a model to reason step by step (Wei et al. 2022), interleaving that reasoning with actions (ReAct; Yao et al. 2022), teaching models to call external tools (Toolformer; Schick et al. 2023), and combining several such agents (Wu et al. 2023), all built on the transformer architecture (Vaswani et al. 2017) and on general-purpose models (Brown et al. 2020; Ouyang et al. 2022; Bommasani et al. 2021; OpenAI et al. 2023), some of which learn to browse and use tools directly (Nakano et al. 2021). In the sciences these agents now run chemistry platforms (Bran et al. 2023; Boiko et al. 2023) and end-to-end research loops (Lu et al. 2024). Beyond their role as literature and reasoning assistants (Leung & Bovy 2024; de Haan et al. 2025), large language models (LLMs) are used in astronomy as agents that call scientific tools and iterate under quality control. These tools are already advancing stellar astrophysics and survey analysis (Ting et al. 2026; Fouesneau et al. 2024; Seeburger et al. 2024).



Two independent groups have published a method for this agent rather than for a human reader: Model Context Protocol (MCP) and Skill. The MCP is an open standard for exposing a capability as a typed tool with declared inputs, outputs, and limits which any agent can call. A Skill is a written record of the operating decisions and their order, given to the agent so that it applies the method the way an expert would. Together, MCP and Skills let us publish a method's know-how alongside its operational code, a form an agent can re-apply to new data.

In this paper we do this for the EB18 SB2 decomposition, packaging it as MCP servers and a Skill and running it as an agent over APOGEE DR19. Our main result is the DR19 catalog, a main-sequence SB2 sample consistent with EB18. A multi-epoch extension refits the individual visits, velocity-confirming 68.5% of the multiply-visited SB2 and adding single-lined velocity variables and orbit-ready systems (Section 4.4). We use the best-sampled systems for a first eccentricity comparison of close twins against non-twins (Section 4.5). We also ask which of the operating decisions an agent could recover on its own. Removing one decision from the Skill

Our Skill records the order and rationale of choices an experienced operator otherwise carries in their head.

[1] https://github.com/kareemelbadry/binspec

We search 238,205 DR19 dwarfs and calibrate on real spectra because realistic residuals create the false positives.

and giving a fresh agent the tools and the ablated Skill separates the know-how that leaves a measurable trace in the fit from the know-how that does not (Section 4.6).

2. DATA

2.1. *APOGEE DR19*

We use the APOGEE arm (Majewski et al. 2017) of the Sloan Digital Sky Survey (SDSS; Blanton et al. 2017) DR19, part of the fifth-generation survey SDSS-V (Kollmeier et al. 2017), recorded with the 2.5-m Sloan Telescope (Gunn et al. 2006) and the APOGEE spectrograph (Wilson et al. 2019) and reduced by the Astra 0.6.0 pipeline into `mwmStar` products (Nidever et al. 2015; Ahumada et al. 2020; Almeida et al. 2023). Each combined spectrum is sampled on an 8575-pixel logarithmic-wavelength grid spanning 15100.8–16999.8 Å. We read the raw flux and inverse variance and do not use the survey continuum, since the normalization is re-derived as part of the fit. The spectra are delivered in the rest frame, with the radial velocity applied upstream. We verified that applying any additional velocity shift to the delivered spectra strictly increases the fit χ^2 (degrades the fit), confirming the rest-frame state.

We select main-sequence dwarfs from the DR19 `the_payne_apogee_star` catalog, whose labels are computed with the method of Ting et al. (2019), requiring surface gravity $\log g$ between 4 and 5, effective temperature $T_{\rm eff}$ between 4000 and 7000 K, and signal-to-noise ratio above 60. This yields 238,205 dwarfs with usable combined spectra, the full sample over which the search is run. The 11,424 primaries below the 4200 K floor of the single-star model (Section 3.1; 4.8% of the sample) are retained because line doubling remains detectable there, but are fit at the floor and carry a larger minimum detectable mass ratio, which we fold into the completeness discussion.

The cool stars stay in the search, but their 4200 K model-floor limitation is carried into the completeness analysis.

2.2. *Validation samples*

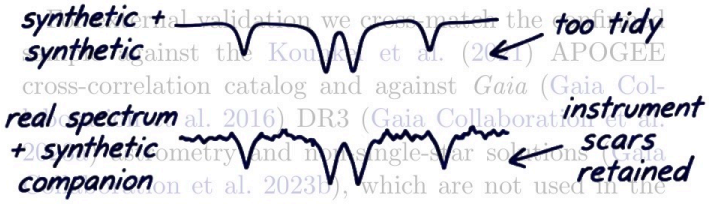
Two labeled sets underpin the calibration of the acceptance thresholds (Section 3.3) and the completeness and benchmark reporting: an enlarged benchmark whose positives are *real* EB18-flagged SB2, and an injection-recovery completeness set. Where we inject, we add synthetic secondaries to *real* single-star spectra, so that the injected composites carry the same instrumental residuals, telluric remnants, and label imperfections that the classifier must survive on genuine data. Injecting secondaries into model spectra instead would omit exactly the structure that generates false positives.

For the benchmark we take the DR19 spectra of the EB18-flagged SB2 that survive our quality cuts, 2,344 systems, as positives, and a matched set of 7,866 non-flagged dwarfs spanning the same signal-to-noise range as controls. The false-positive rate is measured on the held-out controls the classifier never trained on, and this labeled set defines the recovery-versus-false-positive curves of Section 4.1, where the adopted operating point is

Model-into-model injections are too clean; they omit exactly the imperfections that fool the classifier.

For completeness we inject synthetic companions into real single-star spectra and attach a secondary at a grid of mass ratios q and velocity separations Δv, synthesize the isochrone-tied companion with the catalog single-star model (Section 3.1), sum in flux with the luminosity weighting of Equation (1), and add the primary's own inverse-variance noise. The recovered fraction in each $(q, T_{\rm eff})$ bin is the completeness mapped in Figure 11.

Because the companion comes from the same model the classifier uses, the recovered fractions are an upper bound on the true completeness, since a real binary carries line-list and abundance differences that the model does not reproduce and is harder to recover than a model composite. This is the same reason we calibrate the acceptance thresholds on real held-out controls rather than on model injections (Section 3.3). We use this map for the shape of the sensitivity, how the minimum detectable q increases toward cool primaries, and we do not turn it into an absolute multiplicity fraction.



As an external validation we cross-match the confirmed sample against the Kounkel et al. (2021) APOGEE cross-correlation catalog and against *Gaia* (Gaia Collaboration et al. 2016) DR3 (Gaia Collaboration et al. 2023a) astrometry and its single-star solutions (Gaia Collaboration et al. 2023b), which are not used in the spectroscopic detection. Recovery and false-positive rates are quoted with binomial (Wilson) 68% intervals given these sample sizes.

3. METHODS

3.1. *The single-star model*

The classifier accepts a star as a binary when a two-component fit beats the single-star fit. Its load-bearing ingredient is the single-star model, which must predict a normalized spectrum from stellar labels accurately enough that the residual of a genuine single star is consistent with noise. We follow EB18 in building it data-driven, learning the label-to-spectrum map from the survey's own spectra (e.g. Ness et al. 2015; Casey et al. 2016; Ting et al. 2019; Xiang et al. 2019; Fabbro et al. 2018; Leung & Bovy 2019; Allende Prieto et al. 2006; Recio-Blanco et al. 2006; Blanco-Cuaresma et al. 2014) rather than synthesizing it from a model atmosphere and a line list (Castelli & Kurucz 2003; Gustafsson et al.

The classifier learns a single-star spectrum first, then asks whether adding a physically linked companion improves it.

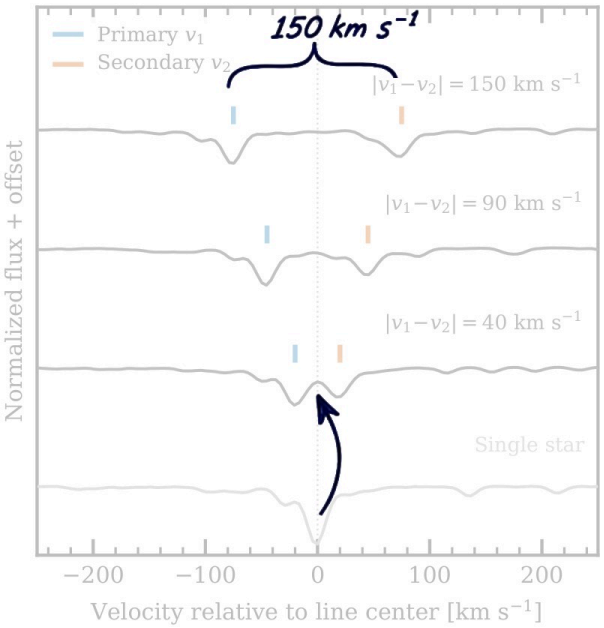
2008; Bergemann et al. 2012), calibrated against benchmark stars (Heiter et al. 2015) and tied where needed to a stellar-evolution grid (Paxton et al. 2011; Dotter 2016); Section 5.3 measures what the synthetic route costs.

For APOGEE we use the five-label network of Ting et al. (2019), a three-layer perceptron that maps the label vector $\theta = (T_{\rm eff}, \log g, [{\rm Fe/H}], [{\rm Mg/H}], v_{\rm macro})$ through two hidden layers of 300 units to a continuum-normalized spectrum $f(\lambda;\theta)$, sampled on the 7,214 continuum pixels of the EB18 normalization and trained with a Huber loss and early stopping. The map runs from labels to spectrum. Fitting a star inverts it, optimizing θ until $f(\lambda;\theta)$ matches the observed spectrum. This single map is the whole of the single-star model, and the two-component composite of Section 3.2 is built by evaluating it once per component. Its label coverage therefore bounds the search. The network has a 4200 K temperature floor, and primaries below it are fit at the floor (Section 2.1), which raises the mass ratio at which their companions stay detectable (Section 4.3).

Training the network requires (label, spectrum) pairs, and the labels are the weak link. The DR19 pipeline labels are produced by a different code, and that mismatch acts as target noise that both blurs the learned map and generates false positives.

We therefore use the network to clean its own training labels, in three steps. A first network is trained on ∼4,800 curated dwarfs with their pipeline labels. This is the open reproduction network examined in Section 5.3. That network then refits, once, the labels of the 7,179 dwarfs of the underlying control sample that a preliminary detection pass with the first network leaves unflagged as candidate binaries. We call these 7,179 stars the refit pool, and split it in half. The catalog network is trained on the refit labels of a random half (3,589 stars). The other half (3,590 stars) is never seen in training and provides the held-out controls on which the catalog's false-positive rate is measured (Section 4.1). The 7,866 benchmark controls of Section 2.2 come from the same underlying control sample and serve the separate purpose of setting the recovery against false-positive curves, so the three counts refer to the refit pool, its held-out half, and the benchmark set in turn.

The refit is anchored, in that the new labels are seeded from and stay tied to the pipeline labels rather than iterated freely, and this is what makes the (label, spectrum) training pairs self-consistent with the model family. Iterating the refit further degrades the classifier, because the labels drift away from their physical anchoring while the fit residual stays flat. The same architecture is used for every variant compared in Section 4.1; its fidelity



velocity separation creates the signal

Figure 1. How an SB2 imprints line doubling, illustrated with a $q = 0.90$ composite model built the same way the classifier builds it (a Sun-like primary combined with a cooler secondary through the isochrone tie), shown around one strong, isolated H-band line. A single star gives one absorption core (grey); as the component velocity separation $|v_1 - v_2|$ grows, the core splits into a resolved pair at the primary (blue) and secondary (orange) velocities. This velocity-dependent doubling, summed over the many lines in the spectrum, is the signal the two-component model captures.

to the data, not the network architecture, is what sets the classifier's performance. The training set, the refit labels, and the trained network are all built from public DR19 data and are released with this work.

3.2. *The forward model and the detection statistic*

The classifier compares two models of the same spectrum: the single-star model above and a two-component composite built from it. The binary composite follows EB18. Two continuum-normalized single-star spectra are summed with a weight set by each component's band luminosity and shifted by the two component velocities,

$$f_{\rm bin}(\lambda) = \frac{w_1\, f_1(\lambda; v_1) + w_2\, f_2(\lambda; v_2)}{w_1 + w_2}, \qquad (1)$$

where $f_{1,2} = f(\lambda;\theta_{1,2})$ are the two components' single-star spectra from the model of Section 3.1, $v_{1,2}$ their line-of-sight velocities, and the weight $w_i = R_i^2\, B_\lambda(T_{{\rm eff},i})$ combines each component's radius R_i with the mean H-band surface brightness $B_\lambda(T_{{\rm eff},i})$ (a Planck factor), turning the surface-area weight R_i^2 into a band-luminosity weight. The temperatures, radii, and hence

The labels were the weak link, so we refit them once to make training targets internally consistent.



Iterating again looked tempting but let labels drift without improving the residuals.

The companion flux is fixed by stellar evolution, preventing an arbitrary second spectrum from soaking up errors.

A genuine SB2 improves many doubled line cores at once, not just one suspicious pixel.

This example is persuasive because the same two-component model repairs three separated wavelength windows.

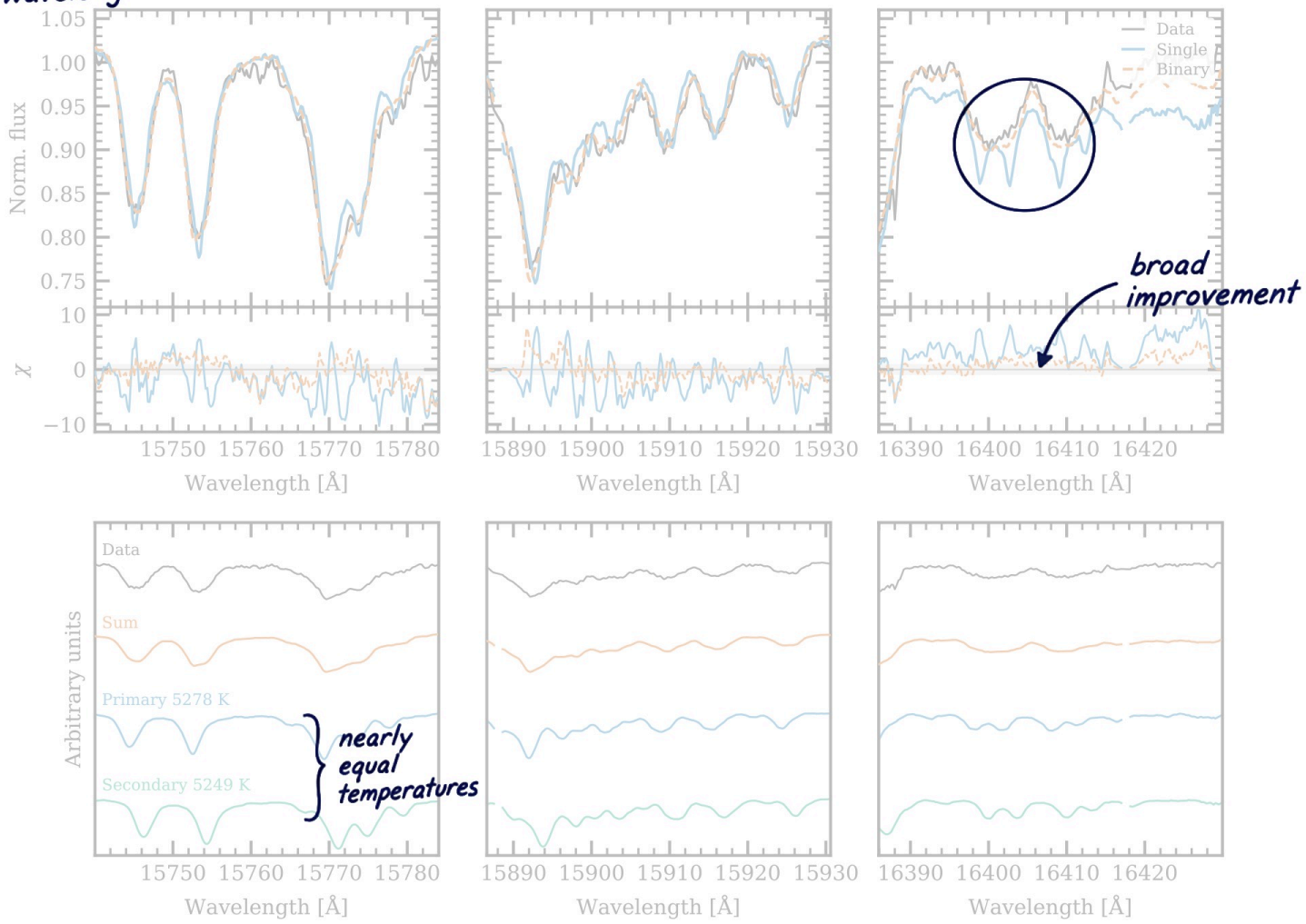


Figure 2. A DR19 dwarf SB2 recovered by the agent (`sdss_id` 116011140, a near-equal-mass pair), at the three H-band windows where the binary model most improves the fit. Top: data with the best single-star (blue) and binary (orange) models. Middle: the χ residuals; the single-star model swings past the $\pm1\sigma$ band at the doubled line cores the binary model captures. Bottom: the two-component decomposition, with the primary and secondary component spectra offset for clarity. The horizontal axis of each column is observed wavelength over one of the three windows.

the weights all follow from the primary and a single mass ratio q through a MIST isochrone (Choi et al. 2016; Dotter 2016) at the primary's metallicity and an assumed common age of 4 Gyr, a representative main-sequence age for the APOGEE dwarf sample, so the flux ratio is fixed by q and not fitted (the isochrone-tied luminosity weighting of Section 3.4). The primary mass M_1 is located on the 4-Gyr isochrone at the primary's ($T_{\rm eff}$, $\log g$, [Fe/H]), the secondary mass is $M_2 = q\,M_1$, and $T_{\rm eff,2}$, L_2, and hence R_2 are read off the same isochrone at M_2, which enforces the coeval, equal-composition pair. The isochrone is evaluated by direct linear interpolation over the MIST main-sequence grid, which is single-valued in mass, with the metallicity and age snapped to the nearest grid nodes; no neural-net emulator is involved, unlike in the `binspec` implementation. At $q = 1$ and zero velocity separation the composite reduces exactly to the single-star model at the primary's labels, and a nonzero separation still leaves the line doubling that the classifier reads. The composite therefore adds only three parameters over the single-star fit, q, v_1, and v_2.

The velocity shift is what the classifier keys on. Once $|v_1 - v_2|$ approaches the instrumental resolution, a single absorption line appears in the composite as a resolved doubled core that splits further as the separation grows (Figure 1). Figure 2 shows one such system recovered from a real DR19 spectrum, with the single- and two-component fits and the implied component decomposition. We optimize the three parameters by a multi-start



one companion explains all three.

Only q, v_1, and v_2 are added; the secondary's temperature and brightness are not freely tuned.

We usually accept a binary only when the fit improves enough and broadly across the spectrum; for $\Delta\chi^2 > 10^5$, the f_{imp} requirement is waived.

search over q and a velocity grid (Section 3.4), holding the primary labels at their single-star values, and retain the maximum-likelihood composite.

The detection statistic is the resulting improvement in fit,

$$\Delta\chi^2 = \chi^2_{\rm single} - \chi^2_{\rm binary} \tag{2}$$

together with the improvement fraction (Eq. B1 of El-Badry et al. 2018b),

$$f_{\rm imp} = \frac{\sum_\lambda \left(|f_{\rm single} - f| - |f_{\rm bin} - f|\right)/\sigma_\lambda}{\sum_\lambda |f_{\rm single} - f_{\rm bin}|/\sigma_\lambda}, \tag{3}$$

where f is the observed flux, $f_{\rm single}$ and $f_{\rm bin}$ the best-fit single-star and binary models, σ_λ the per-pixel uncertainty, and the sums run over all good pixels. The numerator is the reduction in absolute residual the binary model buys over the single-star model, and the denominator is the total difference between the two models, so $f_{\rm imp} \to 1$ when the binary model's departure from the single-star model lands on the data across many pixels. A genuine SB2 improves the fit broadly, across the many line cores the secondary shifts, and so has a large $f_{\rm imp}$. A fake improvement driven by a handful of outlying pixels far from any line has a small one, and is rejected by the improvement-fraction floor of the acceptance ladder. Acceptance is defined by the sliding ladder of Section 3.3, with the rung values recalibrated for the classifier.

$\Delta\chi^2$ alone rewards a few catastrophic pixels; f_{imp} asks whether the binary model moves broadly toward the data.

The same decomposition operates on the individual visit spectra as well as on the combined spectrum, which matters because the two views are sensitive to different systems. A wide or long-period binary whose components barely move over the survey baseline is line-doubled in the coadd and detected there. A close binary, by contrast, can have its components nearly velocity-aligned in one coadd yet well separated in the individual visits, where the orbital motion spreads them across the line profile. Such systems are the ones a single-epoch search misses and a multi-epoch search recovers, and they overlap the radial-velocity-variable population that dominates the close-binary catalogs of APOGEE (Price-Whelan et al. 2020; Kounkel et al. 2021; Mazzola et al. 2020; Daher et al. 2022; Price-Whelan et al. 2018). We therefore also fit the same forward model jointly to a star's individual visits, though our main catalog below is built from the combined spectra alone.

3.3. *The acceptance criterion*

A star is accepted as SB2 when its improvement $\Delta\chi^2$ (single minus binary) clears one of the ladder floors of table B1 of EB18 and its improvement fraction $f_{\rm imp}$ exceeds the paired minimum: from $f_{\rm imp} \geq 0.225$ at $\Delta\chi^2 = 300$ down to $f_{\rm imp} \geq 0$ at $\Delta\chi^2 \geq 3000$. For



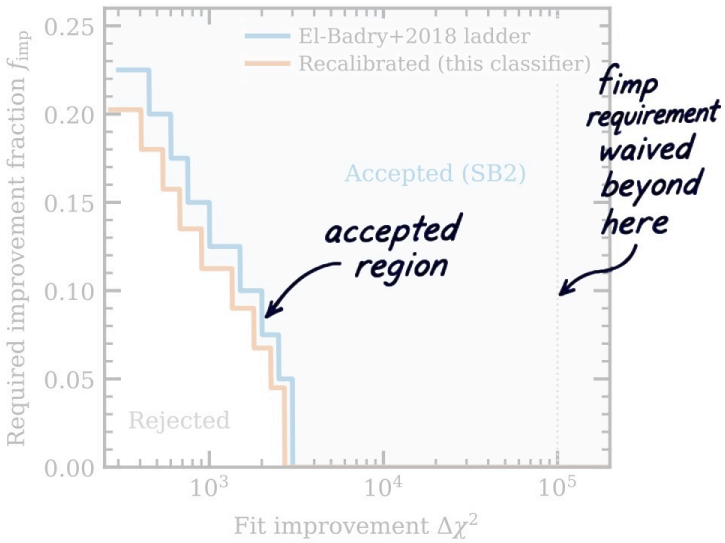


Figure 3. The sliding acceptance criterion. Blue: the EB18 ladder, the minimum $f_{\rm imp}$ required of a star as a function of its fit improvement $\Delta\chi^2$ (the largest floor it clears sets the requirement). Orange: the threshold recalibrated for our classifier (rungs scaled by 0.90 in both coordinates), waived above $\Delta\chi^2 = 10^5$ (grey dotted). A star is accepted as SB2 in the shaded region above the recalibrated threshold.

the catalog the ladder values are recalibrated for our classifier, scaling both coordinates of the rungs by 0.90 (a star passes when $\Delta\chi^2/0.90$ and $f_{\rm imp}/0.90$ clear the published ladder). The scale is chosen at a fixed control false-positive-rate target on one half of the held-out controls and validated on the other, which sets the 8.1% validated rate of Section 4.1. The requirement is waived only for the extreme improvements $\Delta\chi^2 > 10^5$, where even a small $f_{\rm imp}$ reflects a pervasive real mismatch.

For a new survey the *procedure*, calibrating these floors against a labeled benchmark at a fixed control false-positive rate, carries over, while the numerical values are re-derived per instrument (Section 5.3).

3.4. *The operating decisions (the Skill)*

The equations above do not by themselves reproduce the EB18 catalog. What makes the method work is a set of operating decisions, and each one changes the resulting catalog in a way that the equations alone do not reveal. We record them in the Skill as an ordered list, giving for each the choice, the reason, and the failure mode it prevents, so that an agent (or a human) has the *why* as well as the *what*. All eight are written as imperative lines in the Skill, which is released with the software.

Decisions 1, 2, 5, and 8 are also enforced by servers (the shared normalization operator, the single-star

The ladder shape transfers, but its numerical rungs must be recalibrated for each classifier and instrument.

model, the ladder calibration, and the isochrone-tied composite of Eq. 1), so for those the Skill line records a choice the tools also implement. In the blind-agent test, removing a server-enforced decision resets both the Skill line and the server it controls: decision 1 by dropping the self-consistent normalization and decision 8 by disabling the isochrone-tied luminosity weighting in the composite, so the agent must recover the decision from its measurable effect (Section 4.6). The eight load-bearing decisions are the following.

1. *Self-consistent normalization.* The model and the data are normalized by the same operator, so that a continuum error enters $\chi^2_{\rm single}$ and $\chi^2_{\rm binary}$ identically and cancels in $\Delta\chi^2$. Adopting the survey continuum, or normalizing the two sides separately, leaves a residual that the extra freedom of the two-component model absorbs; $\Delta\chi^2$ then reads a normalization mismatch as a detection. This is the single most consequential choice.

2. *A five-label single-star model.* The single-star model spans $T_{\rm eff}$, $\log g$, [Fe/H], and two abundance dimensions rather than the first three alone, because a three-label model leaves residual line structure that the binary model can also absorb, inflating the false-positive rate near the detection threshold.

3. *Pixel masking and a signal-to-noise limit.* Persistently bad pixels are masked and the per-pixel signal-to-noise is capped (at 200 for APOGEE) before the fit. A handful of underestimated error bars at high signal-to-noise otherwise drive $\Delta\chi^2$ upward without any broadband improvement, producing detections localized to a few pixels.

4. *A mass-ratio multi-start.* The fit is restarted from several initial mass ratios, because $\Delta\chi^2(q)$ is multi-modal and a single start settles in the wrong minimum. In particular the $q \to 1$, equal-velocity limit must not be allowed to collapse onto a single velocity-shifted single-star spectrum.

5. *Threshold calibration at a fixed control false-positive rate.* The sliding acceptance thresholds are calibrated against labeled real data rather than on model-into-model spectra: EB18 derived their rung values from semi-empirical injections, and we re-derive the values for our classifier on real held-out controls at a fixed false-positive-rate target (Section 3.3). The *procedure* transfers to a new survey; the calibrated *values* are re-derived per classifier and instrument (Section 5.3).

6. *Completeness over the* $(q, T_{\rm eff})$ *plane.* Completeness is reported as a function of mass ratio and primary temperature rather than as a single number, because the temperature floor of the single-star model raises the minimum detectable mass ratio for cool primaries.

7. *A physical-signature check on the companion.* A candidate whose $\Delta\chi^2$ concentrates on a few detector-edge pixels rather than on the shared line cores that a real secondary produces are rejected by requiring $f_{\rm imp}$ to clear its rung of the acceptance ladder, with the rung values calibrated for the classifier in use at a fixed control false-positive rate, and with the high-$\Delta\chi^2$ waiver of Section 3.3.

8. *Isochrone-tied luminosity weighting.* The flux ratio of the two components is fixed from an isochrone at the shared age and metallicity rather than fitted from the mean continuum, because a continuum-based weight biases the recovered q low at the equal-mass end.

Decisions 1 and 8 bracket the blind-agent test of Section 4.6. The first leaves a large, label-free internal signal that an agent can act on, the second changes only a derived quantity and leaves none.

3.5. *The MCP servers and the agent*

We expose these capabilities as nine MCP servers (Table 1; Figure 4). Each server declares typed tools with [illegible] and returns a compact value rather than a file the agent parses. The science behind them lives in a deterministic module that returns identical results under any agent or under a fixed script, so reproducibility rests on the tools and the Skill rather than on the specific language model.

The agent is a language model primed by the Skill and connected to the servers through a plan–call–observe–decide loop implemented as a small state graph in LangGraph. The graph has one node per stage. A planning node reads the open [illegible] decisions and chooses which tools to call and in what order. A tool-calling node invokes a server through its typed MCP interface and writes the compact return into the shared state. An observation node updates the running hypothesis (single versus binary, and the current best q and velocities). A decision node either requests another tool call or emits the verdict. The loop follows the reason-and-act pattern of Yao et al. (2022) and the learned tool-use of Schick et al. (2023), specialized to a fixed scientific task

Eight operating decisions keep continuum errors, bad pixels, local minima, and implausible flux ratios from masquerading as binaries.

Normalization is the most consequential choice because the extra binary freedom eagerly absorbs continuum mismatch.

Multi-starting q is cheap insurance against a genuinely multimodal fit surface.

The S/N cap is defensive statistics: tiny quoted errors should not let a handful of pixels dominate.

Schematic: one overconfident pixel
Same normalized flux 1; model 0.98
quoted error 0.001
effective error 0.005
flux 1
model 0.98
Cap per-pixel S/N at 200 before fitting
400
chi-square contribution
16
0
Same residual; less excessive weight
fimp is a separate check
Waived only when delta chi-square > 10^5

Nine typed tool servers provide the calculations; the Skill tells the agent how and when to use them.

Table 1. The nine MCP tool servers and what carries over to a new survey. Inputs and returns are abbreviated; every field is typed and carries units. The eight operating decisions and the seven survey-agnostic servers carry over as *procedures*; calibrated numbers (e.g. the ladder thresholds of decision 5) are re-derived per survey by the same recipe.

Server	Representative tool: inputs → returns	Transfers	Role
`data`	`load(id)` → wl, flux, ivar, snr	no	read a survey spectrum
`single_star`	`predict(`$T_{\rm eff}$`,log g,[Fe/H])` → flux	no	single-star spectral model
`binary_model`	`single_vs_binary` → $\Delta\chi^2$, $f_{\rm imp}$, q, v_1, v_2	yes	composite fit + statistic (Eqs. 1–2)
`isochrone`	`secondary(`q`,`$T_{\rm eff}$`)` → $T_{\rm eff\,2}$, ratio	yes	map q to the secondary, any band
`doppler`	`shift(flux,`v`)` → flux	yes	velocity shift on any grid
`broadening`	`convolve(flux,`R`)` → flux	yes	broadening at any R
`gaia_sql`	`xmatch(id)` → ϖ, RUWE, NSS	yes	astrometric cross-match
`gaia_xp`	`overluminous(id)` → ΔM_G	yes	color–magnitude test
`vision`	`inspect(render)` → confidence, flag	yes	read a rendered fit, veto weak
Skill (8 decisions)	written operating decisions	yes	method-level, not instrument-specific

NOTE—Seven of nine servers and all eight Skill decisions are reused unchanged across surveys; the data server is rewritten for the new survey's spectra and the single-star model is replaced by one tuned to the new instrument's flux calibration (Section 5.3).

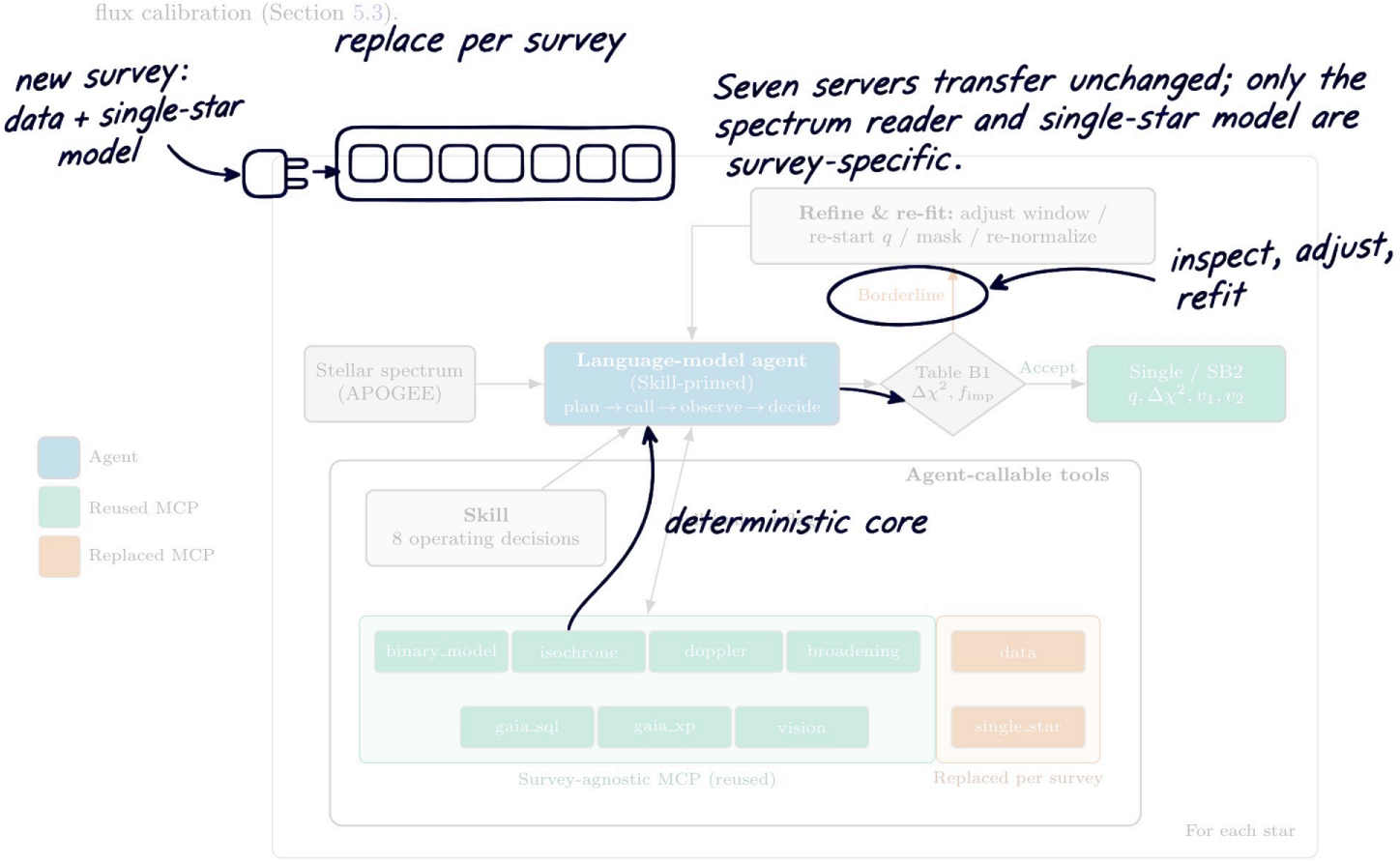


Figure 4. The agent and its tools, as a processing flow. A Skill-primed language-model agent fits each spectrum with a single-star and a two-component model, reads the detection statistic ($\Delta\chi^2$, $f_{\rm imp}$) against the EB18 acceptance gate, and, for borderline cases, inspects the rendered fit and *Gaia* evidence before deciding single versus SB2. Borderline or flagged fits are refined and re-fit before the final accept-or-reject verdict. Green marks the seven servers and the operating decisions that are survey-agnostic and reused unchanged. Orange marks the two components replaced per survey, the data server and the single-star model (Section 5.3).

On held-out stars, the two-number gate separates most known SB2s from controls before the full survey is touched.

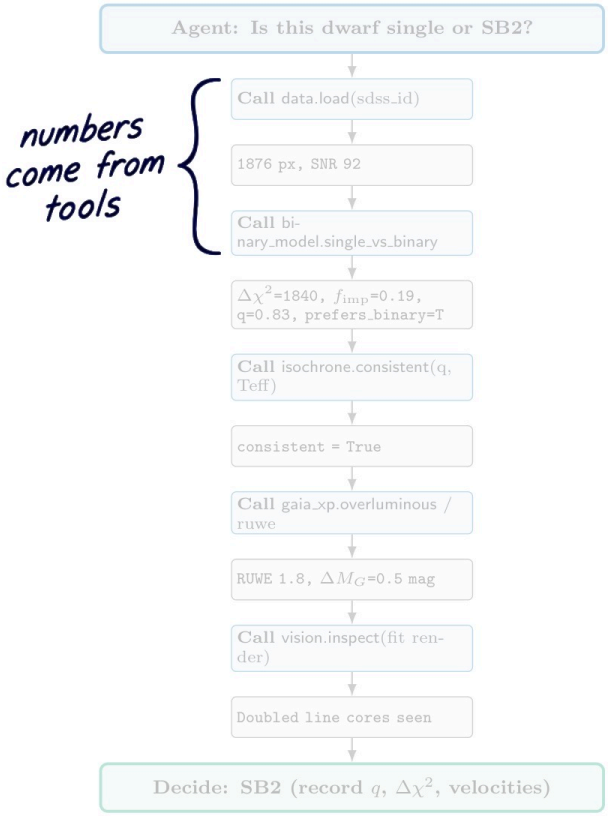


Figure 5. One agent trajectory on a flagged SB2. The agent (blue) calls the tools in order and reads back each compact return (grey), then issues the verdict (orange). The values shown are those the catalog classifier recovers for the system in Figure 2.

and constrained by the Skill so that the model's latitude is in *which* evidence to gather and *when* to stop, not in the numerical results, which come from the deterministic servers.

A vision node reads the rendered single-star and binary fits together with the *Gaia* evidence and flags detections that do not survive inspection, catching near-equal-mass systems and blends that pass the numeric statistics. This is the one node that calls a vision-language model rather than the deterministic core, and it serves the worked examples and the benchmark audit. The full-sample catalog run is deterministic and does not use it. Adding a capability is one server plus one node in the loop, so the system grows by units rather than by rewriting a pipeline. Figure 5 shows one agent trajectory through the first data call to the final SB2 verdict.

Gaia and visual inspection audit examples and borderline cases; they do not drive the deterministic catalog run.



4. RESULTS

4.1. *Benchmark recovery*

Before applying the classifier to the full sample, we validate it on the benchmark of Section 2.2, the 2,344 EB18 flagged SB2 and 7,866 matched field dwarf controls. On this labeled set the two decision statistics can be read against known truth, and recovery can be measured at a controlled false-positive rate, before the classifier is trusted on the unlabeled full sample.

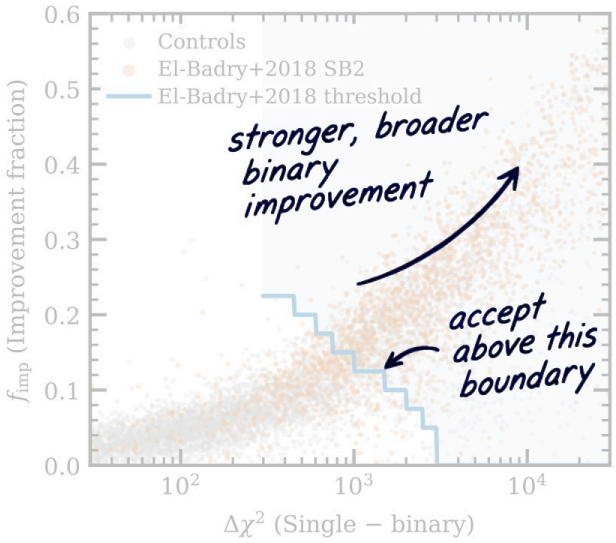


Figure 6. The detection statistic on the benchmark. Each point is one star in the plane of the fit improvement $\Delta\chi^2$ (single minus binary) and the improvement fraction $f_{\rm imp}$. Control stars (grey) stay at low values, while the benchmark SB2 (orange) climb into the acceptance region above the EB18 threshold (blue). These are the two numbers the agent reads back from the binary-model server.

Figure 6 shows the two-number decision on the benchmark. Control stars concentrate at low improvement, while the benchmark SB2 extend along the sliding EB18 ladder into the acceptance region.

Figure 7 shows recovery versus the control false-positive rate on the 2,344-SB2 benchmark. Both the training of the classifier and the calibration of its acceptance thresholds are validated on held-out data. The network is trained on half of the eligible dwarfs and its false-positive rate is measured on controls it never saw, and the recalibrated threshold values are set on one half of those held-out controls and verified on the other.

At the operating point we adopt for the catalog, with the rung values recalibrated for this classifier at a fixed control false-positive-rate target (decision 5), the open real-data classifier recovers 74.4% of the benchmark SB2 at an 8.1% validated false-positive rate. At its loosest setting it reaches 82.6% at 12.3%. Run as a best-case reference on the same benchmark, the EB18 network reaches 75.6% at its loosest 13.3% point and only about 55% at the catalog's 8.1% false-positive rate, so the open classifier exceeds the reference at every matched false-positive rate.

A benchmark is essential here because a plausible-looking fit is not a calibrated detection rule.

At our chosen operating point, recovery is 74.4% with an 8.1% control false-positive rate.

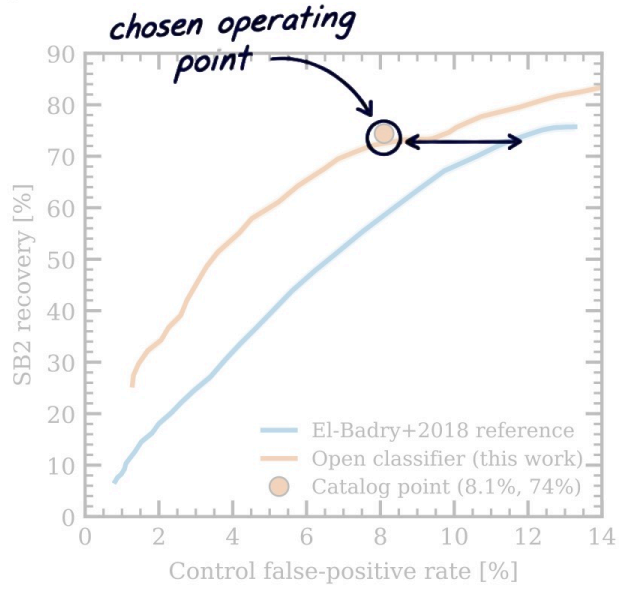


Figure 7. SB2 recovery versus control false-positive rate on the benchmark (2,344 SB2 and, for the false-positive rate, the 3,590 held-out controls the classifier never trained on). Our open real-data classifier (orange) is shown alongside the EB18 network run as a best-case reference (blue). The adopted catalog operating point is marked (8.1% validated false-positive rate, 74.4% recovery); at that false-positive rate the best-case reference recovers about 55%, and at its own loosest setting (13.3%) it reaches 75.6%, which the open classifier exceeds at 82.6% recovery and 12.3%. Bands are 1σ binomial.

Neither classifier recovers every EB18-flagged SB2, and not even EB18's own network run as a best-case reference does. The reason is that the benchmark positives were flagged on the DR13 spectra, whereas we test on the independent DR19 re-reduction of the same stars. The two releases combine a different set of visits and pass through a different pipeline, so a star's DR19 combined spectrum can carry a smaller velocity split, lo[illegible] [illegible] addition the [illegible] shows [illegible] here is therefore measured relative to the DR13 flags, not as an absolute completeness, and the shortfall is a property of the changed data rather than of either classifier.

The older network is a best-case reference, not a perfectly reproducible baseline.

4.2. *The APOGEE DR19 SB2 catalog*

Run over the 238,205 dwarfs under a fixed driver script, the classifier flags 41,466 SB2 (17.4% of the full sample) at the recalibrated acceptance (Section 4.1), which we take as the DR19 SB2 catalog, reporting the detections directly as EB18 did. As set out below, the control false-positive rate implies that close to 40% of these are falsely flagged singles, so the sample is a candidate list rather than a pure catalog. Table 2 lists the released columns.

DR13 labels and DR19 spectra are not identical evidence, so benchmark misses are not pure classifier failures.

Table 2. Released columns of the DR19 SB2 catalog and its supplements. The last five rows (`ruwe` through `sb1`) come with the *Gaia* cross-match and multi-epoch supplement tables released alongside the catalog. Full descriptions and example rows accompany the data release.

Column	Unit	Description
`sdss_id`	—	SDSS-V identifier
`gaia_dr3_source_id`	—	*Gaia* DR3 identifier
`ra`, `dec`	deg	J2000 coordinates
`teff1`, `logg1`, `feh`	K, dex	primary labels
`q`	—	recovered mass ratio
`teff2`	K	secondary $T_{\rm eff}$ (isochrone tie)
`v1`, `v2`	$\mathrm{km\,s^{-1}}$	component velocities (coadd)
`dchi2`	—	$\Delta\chi^2$ (single − binary)
`fimp`	—	improvement fraction
`sb2`	flag	accepted as SB2 (recalibrated gate)
`teff_floor`	flag	primary at the 4200 K model floor
`ruwe`	—	*Gaia* DR3 RUWE
`nss`	flag	*Gaia* non-single-star solution
`n_visits`	—	number of APOGEE visits
`dvmax`	$\mathrm{km\,s^{-1}}$	max. primary velocity change
`sb1`	flag	single-lined variable (supplement)

validation and multi-epoch supplements

The flagged systems span the full APOGEE disk, bulge, and halo footprint, tracing the full dwarf sample with no spatial selection beyond that of the survey itself (Figure 8). This detection rate is comparable to the 13.1% (2,645 of 20,142) of EB18, reached at the benchmark-controlled false-positive rate of Section 4.1 (Figure 7). The median recovered mass ratio is $q = 0.91$, or $q = 0.80$ over the 0.2–0.95 interval where the decomposition is most sensitive, close to the 0.83 of EB18.

As an independent check, following EB18, we place the flagged systems in the *Gaia* color–magnitude diagram (Figure 9). Of the 36,300 with a parallax of signal-to-noise $\varpi/\sigma_\varpi > 5$, 77% lie above the single-star main sequence, the over-luminosity expected of an unresolved binary. Cross-matching the flagged SB2 to *Gaia* DR3, the systems with a RUWE measurement have higher astrometric noise (∼57% with RUWE> 1.4, against ∼20% of a non-flagged control sample) and more non-single-star solutions (∼19% versus ∼4%). About 17% of the flagged systems in the Kounkel et al. (2021) footprint also appear as SB2 there, a lower bound set by that catalog's velocity-separation selection. These independent tracers corroborate the catalog.

The released flags let users trade completeness for purity instead of pretending one threshold suits everyone.

[illegible] spectroscopic follow-up [illegible] both are quoted as fractions of the 41,466 flagged systems, following the EB18 estimates. Chance alignments

purity ← threshold → completeness

8.1%, 74.4%

The candidates trace APOGEE's footprint and show the independent Gaia signatures expected for unresolved binaries.

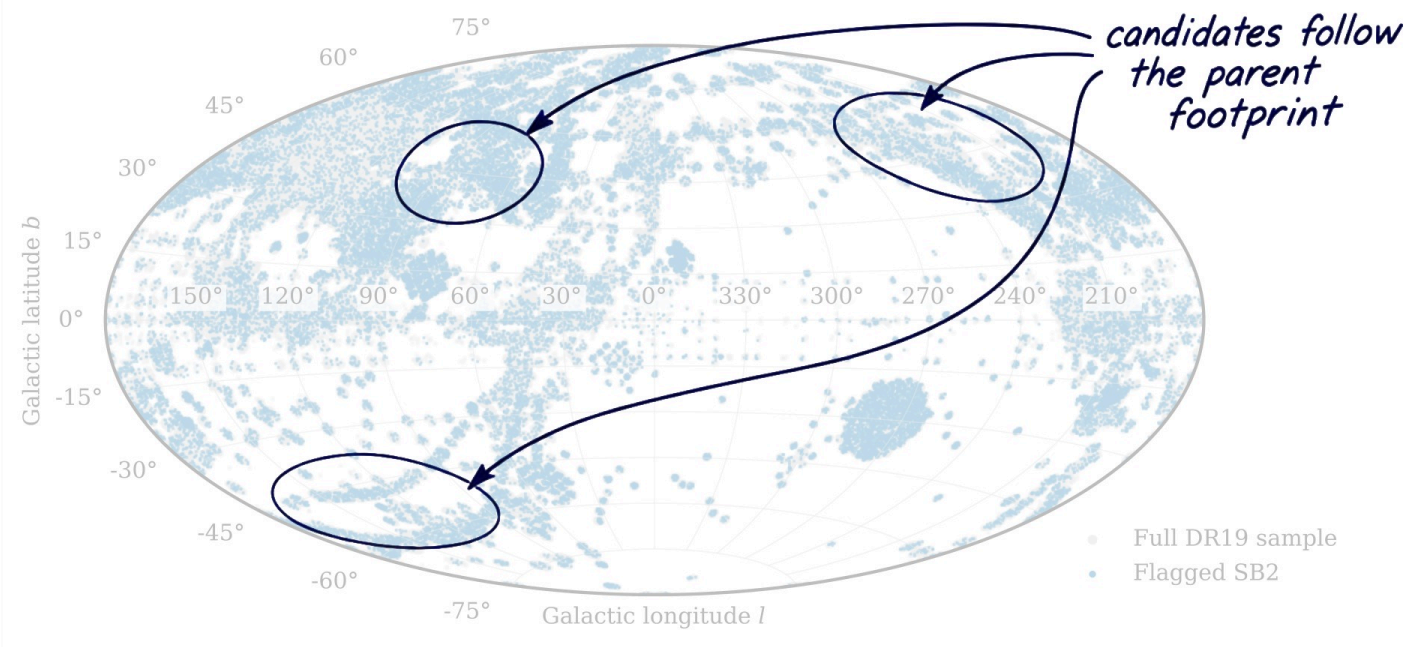


Figure 8. Galactic distribution (Aitoff projection, longitude increasing to the left) of the flagged SB2. Grey: the full DR19 dwarf sample with a coordinate match in the DR19 astra ASPCAP summary; blue: the 41,290 flagged SB2 with a match (of 41,466 flagged in the sample). The flagged stars trace the APOGEE footprint and the Gaia signatures expected for unresolved binaries.

Spatial agreement is a selection check, not proof that each blue point is a binary.

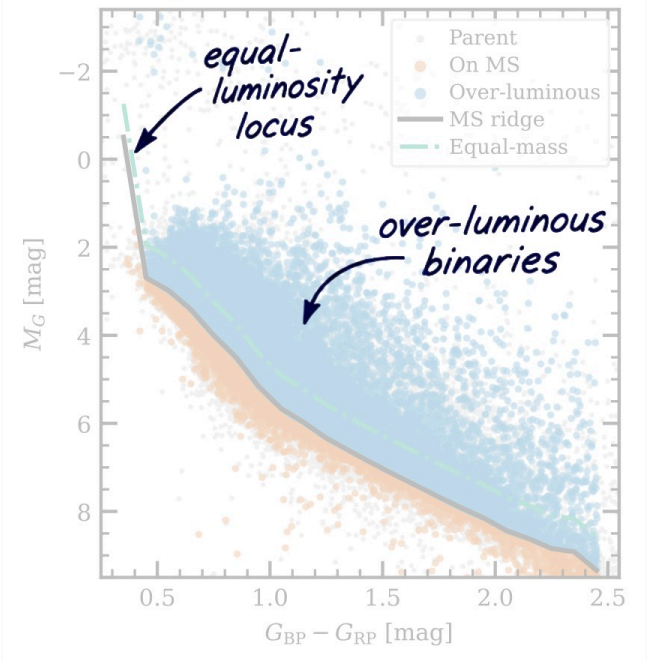
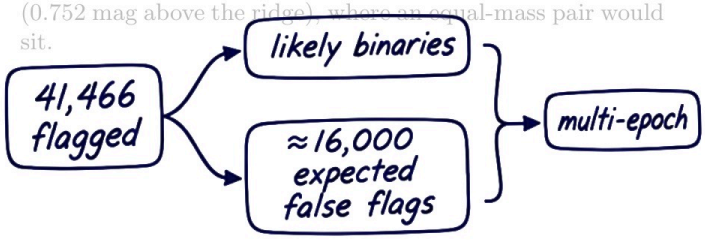


Figure 9. *Gaia* color–magnitude check of the flagged SB2, in observed (not de-reddened) M_G and $G\mathrm{BP} - G\mathrm{RP}$. Grey: the full dwarf sample, whose running median is the main-sequence ridge (black solid). Blue: flagged SB2 above the ridge (77% of those with a reliable parallax), as expected for unresolved binaries. Orange: flagged SB2 on or below the ridge. The green dash-dot line is the equal-luminosity locus (0.752 mag above the ridge), where an equal-mass pair would sit.

within a fiber contribute $\lesssim$1% of the flagged sample and hierarchical triples mis-fit as two components contribute $\sim$3% of it. They land in the catalog at these enhanced rates, rather than at their much lower parent-sample rates, because both produce the near-equal-luminosity composites the classifier selects for. Together they are an order of magnitude below the spectroscopic false-positive term that follows. Read at face value, the 8.1% held-out control false-positive rate applies to the single-star population, which the $\sim$197,000 unflagged dwarfs approximate, and implies of order 16,000 falsely flagged singles if the control rate translates directly to the full sample. Those land inside the catalog, where they would make up close to 40% of the 41,466 flagged systems. The 77% over-luminous fraction (against about half for ridge-like stars by construction of the ridge) and the 68.5% multi-epoch velocity confirmation (Section 4.4) are both consistent with contamination of that order. An external check that does not condition on the spectra points the same way. On a random subsample of the searched dwarfs cross-matched to *Gaia*, the flag rate among astrometrically quiet stars, RUWE below 1.1 and no non-single-star solution, is 9.6 ± 0.5%. Real short-period binaries produce little astrometric wobble and survive that cut, so this rate is an upper bound on the false-positive rate, and it brackets the 8.1% control value from the independent side.



The control rate translates to roughly 16,000 false flags, so purity-sensitive work should use multi-epoch confirmation.

The catalog's apparent mass-ratio and metallicity distributions are shaped as much by detectability as by astrophysics.

supplement. The counts in this paper refer to the full flagged sample, reported at its stated false-positive rate as in EB18.

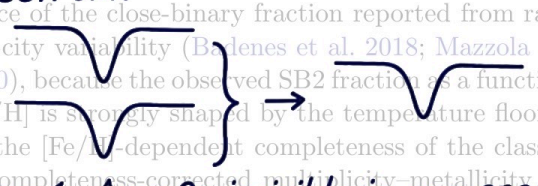
4.3. *Properties of the catalog*

Figure 10 summarizes the catalog. The recovered mass-ratio distribution (panel a) increases toward equal masses, with a peak at the near-equal-mass twins. Part of this peak is expected, since an excess of near-equal-mass pairs is a standard concern for such searches (Price-Whelan & Goodman 2018; Moe & Di Stefano 2017; El-Badry et al. 2019). Part of it is contamination. The falsely flagged benchmark controls concentrate at high mass ratio, with a median q of 0.94 and half above 0.95, because a near-equal composite at small velocity separation is the direction in which the two-component model degenerates toward a single star. Panel a overlays their distribution scaled to the expected number of false positives, which accounts for close to half of the $q > 0.95$ bin. The height of the twin peak should be read with that overlay subtracted in mind. The shape is nonetheless not the intrinsic mass-ratio function, being set also by the classifier's q-dependent completeness and, toward $q \to 1$, by the small velocity split of zero-offset twins.

The high-q peak contains real twins and the easiest false-positive direction; it must not be read raw.

We keep the near-equal-mass twins in the catalog. At $q > 0.95$ the flagged systems have a median velocity separation of 14 $\mathrm{km\,s^{-1}}$ and share the fit statistics of the rest of the sample, so they are line-doubled rather than degeneracies. What stays out of reach is the zero-velocity-offset twin. An equal-temperature pair with no velocity split in the combined spectrum is indistinguishable from a single star there. A close pair whose individual visits show velocity variation is instead recoverable from its per-visit velocities. Only a twin aligned in velocity at every epoch stays unrecoverable, which is why the median-mass-ratio comparison with EB18 (Section 4.2) is made over the 0.2–0.95 range.

A zero-velocity twin is spectroscopically identical to one star in a single combined spectrum.



q = 1, Δv = 0: invisible in one epoch.

In metallicity (panel b) the flagged SB2 track the full sample, peaking near $[\mathrm{Fe/H}] = -0.09$ against -0.11 for the clean sample. We interpret this as evidence for or against the metallicity dependence of the close-binary fraction reported from radial-velocity variability (Badenes et al. 2018; Mazzola et al. 2020), because the observed SB2 fraction as a function of [Fe/H] is strongly shaped by the temperature floor and by the [Fe/H]-dependent completeness of the classifier. A completeness-corrected multiplicity–metallicity measurement requires the two-dimensional selection function we defer to future work.

The velocity separation of the two components in the combined spectrum (panel c) has a median $|v_1 - v_2| = 11$ $\mathrm{km\,s^{-1}}$ and a tail to $\sim$35 $\mathrm{km\,s^{-1}}$ at the 90th percentile. This is the separation at the single epoch of the combined spectrum, not an orbital amplitude. Systems caught near conjunction, where the components are nearly aligned in velocity, are recovered through the line-doubling that the composite model captures even at small separation, and are exactly the systems that a single-epoch cross-correlation search would miss (Zucker & Mazeh 1994). Recovering the orbits themselves requires multi-epoch velocities (Price-Whelan et al. 2017; Pourbaix et al. 2004).

The interplay of these quantities is set by the classifier's sensitivity, which Figure 11 makes explicit in the plane of primary temperature and mass ratio. Warm primaries populate the full range of recovered q, but as the primary cools the minimum recovered q rises. The fifth-percentile q climbs from ≈ 0.6 near 6000 K toward the reliability edge below 4700 K. This is not an astrophysical deficit of low-q companions but the detectability floor of the single-star model, which loses fidelity toward its 4200 K limit so that only the brightest, most nearly equal secondaries still produce a decisive $\Delta\chi^2$. The same trend appears in the injection-recovery completeness set (Section 2.2), and it is the reason we report completeness over the $(q, T_{\rm eff})$ plane rather than as a single number.

The mass ratios translate, through the same isochrone tie the classifier uses, into component temperatures. Figure 12 shows the primary temperature against the secondary temperature implied by the recovered q. The secondaries populate a cooler main sequence below the equal-temperature line, with a median near 4,510 K against 5,460 K for the primaries, so the catalog is predominantly pairs of Sun-like and cooler K-type dwarfs. The lower envelope lifts toward hotter primaries for the same reason the q floor does, since a cool secondary on a warm primary contributes too little light to register.

We therefore report detections, not a completeness-corrected multiplicity fraction.

4.4. *The multi-epoch analysis*

The combined-spectrum search detects SB2 from a single spectrum. Where a star has more than one APOGEE visit, we fit the same forward model jointly to the individual epochs, sharing one set of stellar labels across all visits and tying the two components' velocities at each epoch by momentum conservation about the shared systemic velocity (El-Badry et al. 2018b). This tests the combined-spectrum detections against epoch-to-epoch velocity change and adds single-lined velocity variables the coadd cannot detect. Because the joint fit sums the improvement $\Delta\chi^2$ over all $N_{\rm epoch}$ visits, we scale the acceptance threshold in proportion, requiring $\Delta\chi^2 > 300\,N_{\rm epoch}$ (the single-epoch floor times the

Sensitivity worsens toward cool primaries, while multi-epoch spectra recover velocity information hidden by the coadd.

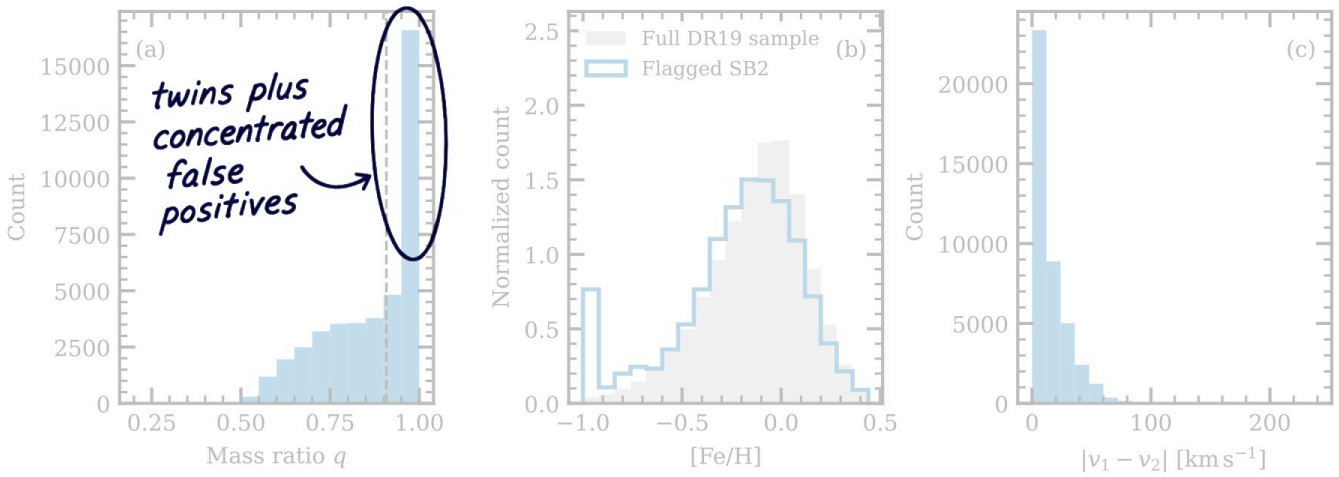


Figure 10. Properties of the 41,466 flagged DR19 SB2. (a) recovered mass ratio q, shown for $q \geq 0.2$ (median dashed). (b) primary metallicity of the flagged SB2 (blue) against the full DR19 dwarf sample (grey), area-normalized; the raw SB2 fraction versus [Fe/H] is selection-dominated and not shown. (c) the implied velocity separation $|v_1 - v_2|$ of the two components in the combined spectrum. All quantities are as recovered by the classifier, not completeness-corrected.

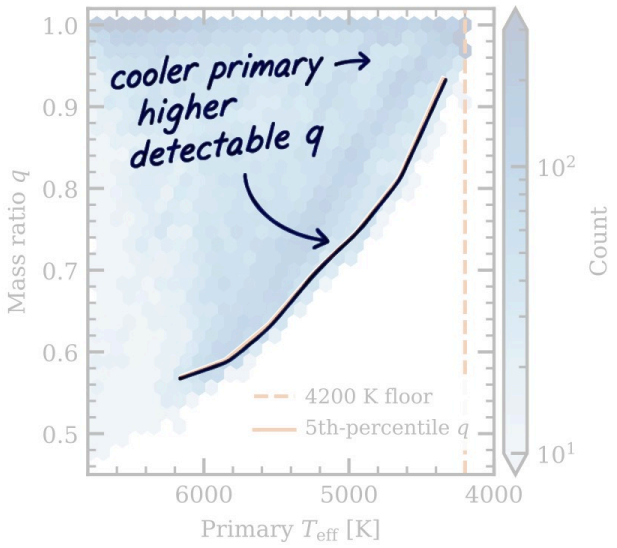


Figure 11. Density of the 41,466 flagged SB2 in primary temperature and recovered mass ratio ($T_{\rm eff}$ increasing to the left; logarithmic color scale). The single-star model's 4200 K floor bounds the recovered mass ratio toward cool primaries (dashed). The fifth-percentile q in bins of $T_{\rm eff}$ (solid) traces the detectability floor: cooler primaries admit only higher-q companions, because the model's declining fidelity toward the floor raises the mass ratio at which a secondary still yields a decisive $\Delta\chi^2$.

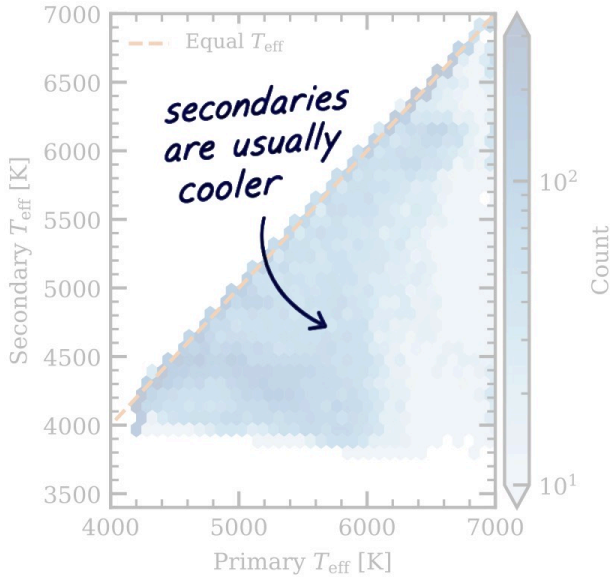
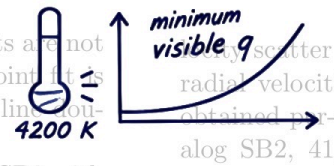


Figure 12. Component temperatures of the 41,466 flagged DR19 SB2: the primary $T_{\rm eff}$ from the single-star fit against the secondary $T_{\rm eff}$ implied by the recovered mass ratio through the isochrone tie (logarithmic color scale). The secondaries lie on a cooler main sequence below the equal-temperature line (dashed), and the lower envelope lifts toward hotter primaries where a cool secondary contributes too little H-band light to be detected.

The rising low-q boundary near 4200 K is a model limitation, not a shortage of low-mass companions.



The temperature wedge is the same selection effect expressed in physical component labels.

number of visits, so that stars with many visits are not flagged from accumulated noise alone. The joint fit is run on dwarfs flagged by combined-spectrum line-doubling or by visit-velocity scatter.

We ran this multi-epoch fit on every catalog SB2 with visit data together with the dwarfs of visit-to-visit ve-

velocity scatter $\sigma_v > 1$ km s^{-1} from the survey per-visit radial velocities), 30,185 unique candidates in total obtained per-visit solutions for 49,595. Among the catalog SB2, 41,164 of the 41,466 (99%) have a fit; the remaining 302 have individual-visit spectra that are absent from the archive or unusable, so they carry only

We scale the multi-epoch $\Delta\chi^2$ threshold with visit count so accumulated noise does not become evidence.

Repeated visits independently confirm most candidates and expose 519 single-lined variables the coadd cannot identify.

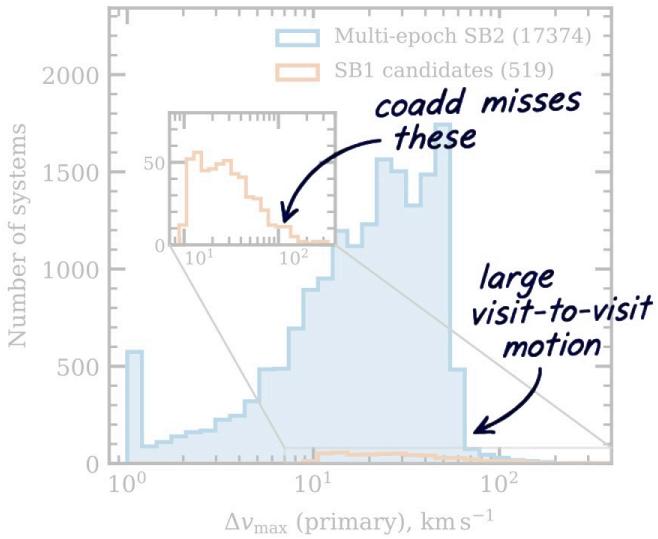
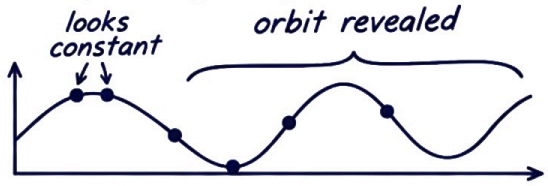


Figure 13. Maximum primary radial-velocity change $\Delta v_{\rm max}$ across visits in the multi-epoch analysis, restricted to systems with three or more epochs, for which $\Delta v_{\rm max}$ is a tracer of orbital motion (two-epoch systems often sample similar orbital phases and are excluded here). The primary velocity is measured at every epoch. Blue: the 17,374 multi-epoch SB2 (both components tracked), whose distribution extends above 100 km s^{-1}. Orange: the 519 single-lined velocity variables (SB1 candidates), selected to have $\Delta v_{\rm max} > 10$ km s^{-1}, the class the combined-spectrum catalog cannot flag; the inset expands their histogram (zoom region boxed).

their coadd detection. The confirmation statistics below use the 26,239 of these with two or more epochs, the rest being single-visit stars whose joint fit reduces to one epoch and cannot test velocity change. Across the sample the median dynamical mass ratio, from the per-visit velocity amplitudes, is 0.90, matching the 0.91 of the combined-spectrum catalog.

First, the multi-epoch fit confirms the combined-spectrum SB2 without using the coadd. Of the 26,239 catalog SB2 with two or more epochs, the per-visit joint fit prefers the two-component model for 68.5%, with a median primary-velocity change of 16.7 km s^{-1} across visits. That rate rises with the number of epochs, from 52.5% at two visits to 71.9% at three, 73.5% at four or five, and 82.0% at six to eight, which is where this fit stops, since it caps at eight visits. A pair of visits at similar orbital phase cannot show a velocity change, so the aggregate rate understates the confirmable fraction, and its complement is an upper bound on contamination rather than a measurement of it. The eccentricity sample of [illegible] fits a single visit instead, so [illegible] the two tra[illegible] quantity. The flagged sys[illegible], as expected for unresolved bi-

Two visits can land at similar orbital phase, so non-confirmation is only an upper bound on contamination.



naries (Figure 13). In that figure the 17,374 systems with three or more epochs are those with per-visit two-component solutions tracking both components. For the best-sampled systems the two components show anti-phase velocities, and the slope of the secondary velocity against the primary recovers the mass ratio (Figure 14).

Second, the fit recovers systems the coadd misses. We find 519 dwarfs that are single-lined but velocity-variable (one set of lines whose velocity shifts by more than 10 km s^{-1} across three or more visits) and not in the SB2 catalog, the SB1 class the combined-spectrum search cannot flag. They are released in the multi-epoch supplement, marked by its `sb1` flag. This search runs only on the σ_v-triaged multiply-visited dwarfs, not on the full 238,205, so its count is comparable to the 663 SB1 of EB18 rather than scaling with the fifteen-fold larger SB2 catalog. And 8,981 of the multi-epoch SB2 have three or more visits spanning more than 20 km s^{-1} in primary velocity, enough phase coverage to anchor a spectroscopic orbit. For comparison, EB18 solved 64 orbits in DR13, although that is a count of fitted orbits rather than of orbit-ready systems.

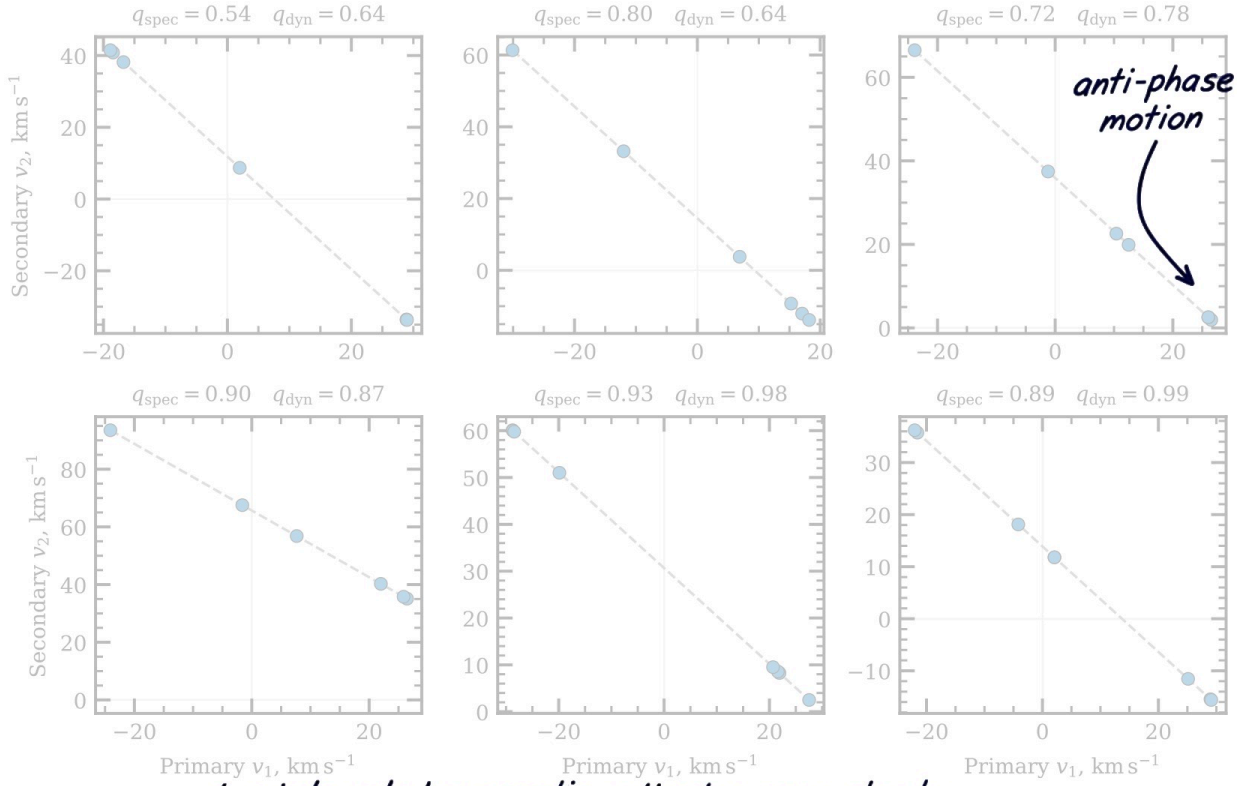
The 8,981 orbit-ready systems are not fitted orbits yet; they simply have useful velocity span and cadence.

4.5. Eccentricities of the close twins

The visit-level [illegible] more population measurement. At wide separations, twin binaries ($q > 0.95$) are far more eccentric than their non-twin peers, an excess that was measured from *Gaia* astrometry (Hwang et al. 2022a) and has been read as evidence that twins form in circumbinary disks at close separation and are widened afterwards (Hwang et al. 2022b). That measurement concerns separations of hundreds to thousands of au. The eccentricities of the close twins themselves, the regime in which the formation picture places them, have not been measured, and our SB2 sample reaches exactly that regime, since the periods we probe below correspond to separations of roughly 0.08 to 1.2 au, some three orders of magnitude inside the wide-twin measurement.

For the multi-epoch SB2 with eight or more visits we refit every archived visit and read the eccentricity from the shape of the two velocity curves. For each system we form the likelihood of its per-visit velocities as a function of eccentricity, with the other orbital elements integrated over and the velocity amplitude and systemic velocity solved in closed form (Appendix A). This gives one curve per system, the eccentricity likelihood, which does not yet involve the population. The population enters through a single index α, with $f(e) \propto e^{\alpha}$, and we give the twins and the non-twins each their own α and compare the two. We keep the 2,009 systems with median periods between 6 and 400 days.

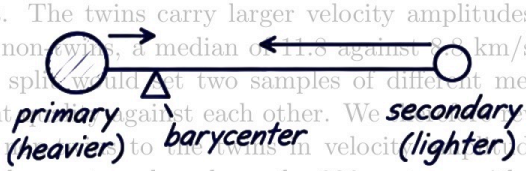
Anti-phase component velocities verify bound pairs and let us compare spectroscopic with dynamical mass ratios.



two independent mass-ratio estimates agree closely

Figure 14. Per-visit component velocities for six example multi-epoch SB2, one per panel. As the primary velocity v_1 increases, the secondary velocity v_2 decreases: the two stars move in anti-phase about the barycenter, as expected for a bound pair. The slope of v_2 against v_1 is $-m_1/m_2$, so its magnitude gives a dynamical mass ratio $q_{\rm dyn}$ (dashed fit) that tracks the combined-spectrum value $q_{\rm spec}$. These are examples selected for good phase sampling, not a population sample.

The inverse magnitude of the dashed-line slope gives the displayed mass ratio $q = m_2/m_1$.



The inner binary of each orbit is sampled at low amplitude near the sampled orbit spends most of its phase near apocenter, where the velocities move little, and it reads as more eccentric than it is. The twins carry larger velocity amplitudes than the non-twins, a median of 41.3 against 29.1 km/s, so a raw split would set two samples of different measurement precision against each other. We therefore weight the fit to the twins in velocity amplitude and epoch count, and we keep the 896 systems with a primary amplitude above 12 km/s, 495 of them twins. On mock populations built at the real cadence the estimator carries a known difference through with a slope near 0.9 (Figure 15), and putting the same index into both samples with the real twin and non-twin sampling returns -0.02 ± 0.03, so the matching adds no difference of its own.

On the real systems the twins fall below the non-twins, with $\alpha_{\rm twin} = +0.15$ and $\alpha_{\rm non\text{-}twin} = +0.41$, and after the injection-test residual is removed the difference is $\alpha_{\rm twin} - \alpha_{\rm non\text{-}twin} = -0.24 \pm 0.16$, where the error combines a bootstrap over systems with the scatter of the injection test and of the matching choices. The value moves by less than 0.1 when we match on period instead of amplitude, drop the systems below the 15-day tidal circularization boundary (Meibom & Mathieu 2005), match on observed quantities alone, or keep only the systems both trained detectors flag, so the choices do not drive it. In mean eccentricity the two samples sit at 0.51 and 0.56, both inflated by the same apocenter effect, so only the difference should be read. The interval reaches zero at 1.5 standard deviations, so the sample does not separate the two classes.

The two classes are therefore close in eccentricity, with a slight preference for the twins to be the more circular, of the sign that circularization of the more processed population would leave. An excess of the wide-binary sign is what the data exclude, since a positive $\Delta\alpha$ above $+0.15$ falls outside two standard deviations for every choice above, while the wide twins at 400 to 1000 au carry an index near 2 against about 1 for their non-twins (Hwang et al. 2022b), a difference of order $+1$ that Figure 15 shows our mocks would recover. Whatever makes the wide twins eccentric is therefore not present at these separations, which supports the picture in which the excess is acquired during the widening rather than

We match twins and non-twins in amplitude and epoch count before comparing eccentricities.

Only the differential eccentricity is robust because missing per-visit errors shift both absolute estimates.

Close twins show no significant eccentricity excess, unlike wide twins, and the agent only rediscovers missing choices with visible diagnostics.

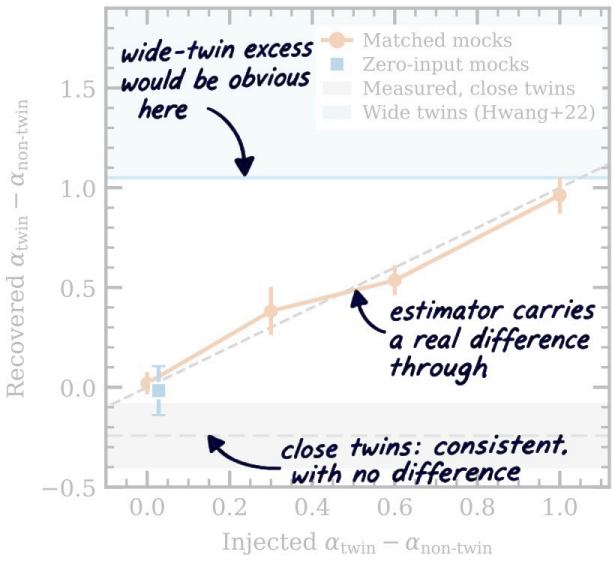


Figure 15. Injection test of the eccentricity-index difference between the close twins and the matched non-twins. Mock populations with a known difference (orange) are recovered along the one-to-one line, and mocks with a zero difference at the real sampling (blue, offset for clarity) scatter around zero. The measured value, -0.24 ± 0.16 (grey band), is consistent with zero, while the difference of the wide twins (blue band, Hwang et al. 2022b) is of order +1 and would have been recovered.

The measured difference is slightly negative but reaches zero within 1.5 standard deviations.

4.6. *The blind-agent test*

The Skill records the operating decisions. A separate question is whether an agent could recover one on its own. We test this by removing one decision at a time from the Skill and handing a fresh agent the tools and the ablated version, with no access to the published answer, to see whether it rediscovers what was removed. We try two decisions that behave very differently.

Removing the self-consistent normalization (decision 1) normalizes the model and data with different operators, so every fit degrades. The median single-star χ^2 over the controls rises from 2.1×10^4 to 6.2×10^4 for a few-percent continuum mismatch and to 2.4×10^5 for a larger one, a jump of a factor of three to more than ten that is plain in the controls alone, with no external label. The control false-positive rate, by contrast, does *not* rise: it falls, from 12% to 3% on the ablation's 250-star control subset (drawn at random from the benchmark controls) at the fixed acceptance, because the shared continuum error inflates the single-star and binary fits together and largely cancels in $\Delta\chi^2$.

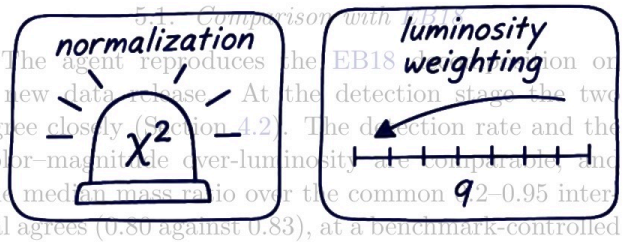
Two ablations illustrate a boundary, not a general success rate for autonomous rediscovery.

The signal the agent has to work with is therefore the absolute fit quality, and it is enough to act on. In a demonstration run, an agent given the high χ^2 rederived the common normalization. Because that signal is deterministic, we report it directly rather than as a success rate over many runs. The demonstration is a single run under a single model, and the two decisions below are the only ones we ablated, so the pattern is an illustration rather than a rate.

Removing the luminosity weighting (decision 8) behaves the opposite way. It biases the recovered mass ratio low, by up to 0.2 at the equal-mass end, but leaves the fit quality and the acceptance unchanged, so nothing internal to the fit marks the choice. Without an external mass-ratio reference the agent has no signal to act on, and the decision goes unrecovered.

Removing common normalization screamed through χ^2; removing luminosity weighting silently biased q.

5. DISCUSSION



5.1. *Comparison with EB18*

The agent reproduces the EB18 detection on a new data release. At the detection stage the two agree closely (Section 4.2). The detection rate and the color–magnitude over-luminosity are comparable, and the median mass ratio over the common 0.2–0.95 interval agrees (0.80 against 0.83), at a benchmark-controlled false-positive rate (Section 4.1). The DR19 catalog is about fifteen times larger in count, against a twelvefold growth of the searched dwarf sample from DR13 to DR19 (238,205 versus 20,142). The modest excess over the survey growth reflects the recalibrated classifier's higher benchmark recovery at the catalog operating point (74.4% against about 55% for the reference at the same 8.1% false-positive rate; Section 4.1). The color–magnitude over-luminosity (Section 4.2) is a consistency check on a shared forward model, not an independent validation, because two selection-limited recovered distributions from the same model are expected to agree. The genuine external anchor is the *Gaia* enrichment, the higher astrometric noise and non-single-star fraction of the flagged systems, drawn from data the decomposition never sees. The catalog also probes a different population from the radial-velocity-variability samples that dominate recent APOGEE multiplicity work (Kounkel et al. 2021), which register a system only when its components are velocity-separated, whereas the combined-spectrum decomposition detects the two-temperature composite even at zero offset. The ∼17% overlap (Section 4.2) is the expected consequence of that difference, not a purity measurement, all the more so as Kounkel et al. (2021) work in the earlier DR16/17 reductions while our search is on DR19.

The main bottleneck is the single-star spectral model, whose imperfections can make ordinary stars look composite.

5.2. *Limitations*

Four inputs set limits we have not removed. The component temperatures and mass ratios come from a fixed 4 Gyr solar-scaled isochrone, applied to a sample spanning disk, bulge, and halo, so the released q and $T_{\rm eff,2}$ carry an age systematic we have not propagated, and the 0.01 mass-ratio floor of Section 3.5 is set by it. The 11,424 primaries at the 4200 K model floor are fit with labels the grid cannot reach, and we mark them with the `teff_floor` flag in the release so they can be cut. The systems with eight or more visits come from the higher-cadence APOGEE fields, which include cluster and calibration pointings and are not a random draw from the survey, and we have not checked their cluster membership. Finally, EB18 do not publish a control false-positive rate in a form matched to ours, so the comparison of our 17.4% flagged fraction with their 13.1% is between operating points of unknown relative purity.

The fixed 4 Gyr isochrone makes q practical, not age-systematics-free.

The catalog is a set of spectroscopic detections, not a corrected multiplicity census. We report what the classifier flags and do not convert it into a completeness-corrected multiplicity fraction. That inference requires the two-dimensional $(q, T_{\rm eff})$ selection function characterized in Section 4.3 and Section 2.2, and we leave it to future work.

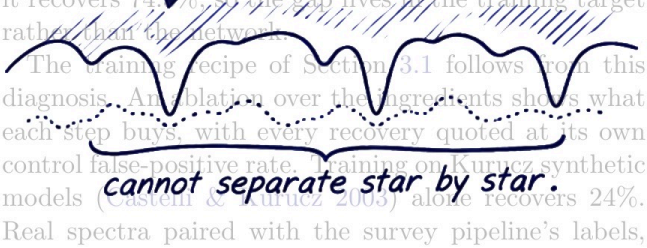
The current tool set implements the single-versus-binary decomposition and its multi-epoch confirmation. In DR13, two higher-order classes were also fit from the 20,142 dwarfs (EB18), 663 single-lined (SB1) velocity-variable binaries and 114 triple-lined (SB3) systems. Our multi-epoch velocity analysis matches the first class with its 519 SB1 (Section 4.4). We do not match the second. We built the three-component extension and attempted the census, and it does not work on the DR19 products. A faint third star changes the spectrum by a few percent, and the single-star model trained on the public DR19 labels misses real spectra at a comparable level, so we cannot separate the two star by star. The limit sits in the training labels rather than in the spectra, and the same label noise is one reason the eccentricity comparison of Section 4.5 uses the twin against non-twin differential rather than per-system eccentricities. We plan to improve the training labels next, and with them the triple census and the per-system orbits. The 8,981 multi-epoch systems with enough phase coverage already hold the velocities for those orbits, through the estimator of Appendix A. Meanwhile our pipeline either catches a triple as an SB2, when two of its components dominate the light, or rejects it at the acceptance gate, when the third component's light dilutes the fit improvement below the threshold.

We attempted a triple-star census; DR19 label noise was comparable to the faint third star's signal.

5.3. *Single-star model quality and survey transfer*

How well the whole system works on a survey is set by the quality of one component, the single-star spectral model. The decomposition flags a binary only when a genuine single star fits the single-star model down to the noise, so a model that reproduces real spectra poorly makes almost every star look faintly composite and blunts the single-versus-binary decision.

EB18 built this model data-driven, training a network on a curated set of real APOGEE spectra. Reproducing that route from public ingredients recovers only 63.0% of the benchmark SB2 at a common 13.3% control false-positive rate, well short of the 75.6% reached by the EB18 network run as a best-case reference on the same benchmark (Section 4.1), even though the two fit the SB2 spectra to the same residual (∼0.83%). This open reproduction is the first-step network of the training chain in Section 3.1. The gap is in single-versus-binary discrimination rather than fit accuracy, and it points to the tacit curation the open reproduction does not carry. EB18 vetted their training sample by eye and censored contaminated or mislabeled stars before the network ever saw them. Label quality plausibly contributes as well, because the public DR19 labels used as training targets may carry more scatter than those of earlier releases such as DR13–14, and a network trained on noisier labels learns a fuzzier label-to-spectrum map. A distillation diagnostic locates the cause. When the same architecture is trained instead on noise-free, label-consistent spectra generated by the EB18 network itself, it recovers 74.4%, so the gap lives in the training target rather than the network.



The training recipe of Section 3.1 follows from this diagnosis. An ablation over the ingredients shows what each step buys, with every recovery quoted at its own control false-positive rate. Training on Kurucz synthetic models (Castelli & Kurucz 2003) alone recovers 24%. Real spectra paired with the survey pipeline's labels, which come from a different code than the network, reach 54–63%. Refitting those labels with the network itself makes them self-consistent and yields the catalog model, which recovers 69.5% at the original EB18 acceptance thresholds. Those thresholds were tuned for the EB18 network and leave ours at a 6.9% false-positive rate, short of the 8.1% we allow, so recalibrating them to the 8.1% target (decision 5) moves the same network to the catalog's 74.4%, above the best-case reference at every matched false-positive rate (Section 4.1). This self-consistency between the labels and the model is what gave the EB18 network its edge, because their training labels were their own model's fits.

Self-consistent refitted labels improved discrimination more than changing the network architecture.

Across surveys, the procedure transfers; the instrument-specific single-star model must be rebuilt and recalibrated.

This single-star model is also the only part of the system tied to a specific instrument, through its line list, its spectral resolution, and the stars it was trained on, so it is the only part that does not transfer unchanged, and the recovery gap at equal fit quality above is what that costs. Moving to a new survey therefore means rebuilding this one model. The other seven servers and the whole Skill carry over unchanged, and the data server is a straight swap (Table 1). An empirical demonstration on a second survey is left to future work.

Equal residual accuracy did not guarantee equal binary discrimination; training-target consistency mattered.

5.4. What kind of know-how could and could not be recorded

The operating know-how behind a method like this falls into three categories that behave differently under transfer:

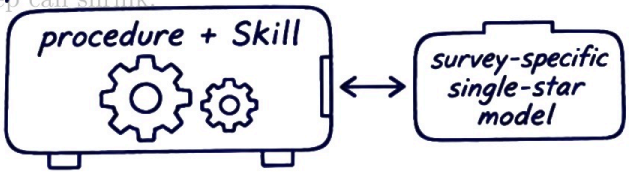
- *Codified* know-how is the equations and the acceptance thresholds: it is fully portable and is what a paper already communicates.
- *Procedural* know-how is the order of operations and the decisions of Section 3.4, the normalization convention, the masking, the multi-start, the calibration recipe: it is portable once written down, which is what the Skill does, but is normally left implicit.
- *Calibrated* know-how is the survey-specific numbers, chiefly the single-star model that reproduces one instrument's spectra: it does not transfer at all and must be rebuilt, as discussed in Section 5.3.

What an agent can recover of this on its own falls along the same lines. The blind-agent test (Section 4.6) probes the boundary between the procedural and calibrated categories. An agent recovers procedural know-how that leaves a measurable trace, such as the normalization whose absence inflates the single-star fit χ^2 on every control, and cannot recover calibrated know-how that needs an external anchor, such as the luminosity weighting whose absence is invisible without a mass-ratio reference.

The procedural layer is itself uneven. Some of it is published but scattered across the source paper, the label pipeline, and the reduction, so an agent that reads across all of it could in principle reassemble it, while some is genuinely tacit, like the priors for iterative clean-star selection and the judgment that recognizes an overfit. Automating the survey-specific calibration as a control, verified by held-out recovery on labeled benchmarks, would push this boundary and test capability, and the direction in which the next survey human step can shrink.

An agent can recover only missing knowledge that leaves an observable trace or has an external reference.

Think of the method as portable procedure wrapped around one replaceable instrument model.



This taxonomy is not special to binary detection. The same split, portable procedure versus instrument-specific calibration, appears wherever a data-analysis method is moved between facilities, and the practice of packaging the procedural layer as machine-runnable tools plus a written Skill is the same one now emerging around scientific agents in other domains (Bran et al. 2023; Boiko et al. 2023; Lu et al. 2024; Ting et al. 2026). In an era in which agents increasingly execute analyses, we expect the procedural layer, long left implicit, to be written down and published as a first-class artifact.

6. CONCLUSION

Over the 238,205 main-sequence dwarfs of APOGEE DR19, the EB18 decomposition identifies 41,466 double-lined spectroscopic binary candidates, 17.4% of the searched sample and about fifteen times the largest previous APOGEE SB2 catalog, against a twelvefold growth of the searched sample since DR13. The classifier reaches this at a validated 8.1% control false-positive rate, with a benchmark recovery that exceeds the EB18 network at every matched false-positive rate. The catalog is characterized by:

- a mass-ratio distribution that rises toward equal masses, with median $q = 0.91$ (0.80 over the 0.2–1.0 range) where the decomposition is most sensitive, and a twin fraction of 23.5% ± 0.5% twin excess;
- component temperatures, tied through the isochrone, that pair Sun-like primaries (median $T_{\rm eff} \approx 5{,}460$ K) with cooler K-type secondaries (median $T_{\rm eff} \approx 4{,}510$ K);
- independent *Gaia* corroboration, with 77% of the systems that have a reliable parallax sitting above the single-star main sequence, elevated astrometric noise (57% at RUWE$>$ 1.4 against 20% of controls), and more non-single-star solutions (19% against 4%);
- a multi-epoch supplement that velocity-confirms 68.5% of the multiply-visited SB2, adds 519 single-lined velocity variables the coadd cannot flag, and identifies 8,981 systems with enough phase coverage to anchor a spectroscopic orbit, against the 64 orbits solved in DR13, a count of orbit-ready systems rather than of fitted orbits;
- no significant difference in eccentricity between the close, well-sampled twins and matched non-twins, -0.24 ± 0.16 in the population index, which excludes at these separations a twin eccentricity excess of the sign found at wide separations by Hwang et al. (2022b).

The release includes the candidate catalog, multi-epoch products, tools, Skill, and deterministic code needed to reproduce the search.

This is the largest sample of double-lined spectroscopic binary candidates assembled from APOGEE, released with per-system mass ratios, component velocities, and *Gaia* and multi-epoch flags for higher-purity selection. At the control false-positive rate it carries of order 16,000 falsely flagged singles, so users who need purity rather than completeness should cut on those flags.

The catalog was produced without re-deriving the method, by publishing its operating know-how rather than only its equations, packaged as agent-callable MCP tool servers and a written Skill of the decisions that make it work. An ablation of two decisions illustrates that this know-how is what carries the method, with a fresh agent recovering a removed decision when its absence leaves a recoverable trace in the data.

For high purity, start with the multi-epoch flags rather than the full 41,466-object list.

Adapting the pipeline to a new survey unchanged. Only the single-star template grid, which carries one instrument's flux calibration, must be rebuilt (Table 1). Automating that last step as a verify-gated loop, with recovery on a labeled benchmark as the objective, is the clearest path to a binary classifier that opens on any survey with no human in the per-survey path, from the other SDSS-V spectroscopic programs (Kollmeier et al. 2017) to the optical surveys that share the composite-fitting logic but not the wavelength range, LAMOST, WEAVE, 4MOST, and the *Gaia* RVS spectra (Cui et al. 2012; Jin et al. 2024; de Jong et al. 2019; Recio-Blanco et al. 2023).

More broadly, as language-model agents begin to carry out analyses, we expect the operating know-how of a method, long left implicit in code and expert practice, to become a research product in its own right. Publishing a method for an agent to run will increasingly mean publishing the decisions that make it work, alongside the equations.

The language model orchestrates and audits; every reported catalog number comes from the deterministic core.

With the MCP servers, the Skill (which operational decisions are enumerated in Section 3.4), the DR19 SB2 catalog with its multi-epoch supplement and column descriptions, the orbit posterior summaries of the systems with eight or more visits, which carry the per-system eccentricity likelihoods under the uniform prior and are therefore unaffected by the population normalization of Appendix A, and the benchmark star list are released at https://github.com/seratsaad/agent4binary. The APOGEE DR19 spectra are public through the SDSS archive, and the catalog classifier is built entirely from public DR19 data, with the training manifest, the refit labels, and the trained network weights all released.

The catalog is produced by a deterministic science core, the single-versus-binary fit, the detection statistic, and the acceptance gate and multi-epoch confirmation behind it, and is reproducible from these servers under a fixed driver script. The language-model agent orchestrates and audits this core rather than replacing it, and where it runs, on the benchmark and the worked examples, it uses `gemini-2.5-flash`, so every number we report reads out of the deterministic core and does not depend on the choice of language model. The one component we cannot redistribute is the EB18 reference network used for the benchmark comparison. Its `binspec` code and method are public, but its trained weights and curated training set are not ours to share, so the reference recovery numbers can be checked against our figures but not retrained from the released tools.

The unavailable EB18 weights affect only the reference comparison, not reproduction of our catalog.

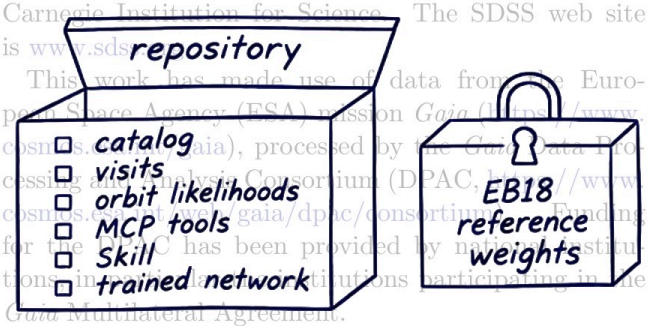
ACKNOWLEDGEMENTS

We thank Hans-Walter Rix and Kareem El-Badry for reading the manuscript and for their comments. SMS is supported by the Distinguished University Fellowship awarded by The Ohio State University. YST is supported by NSF under Grant AST-2406729 and by a Humboldt Research Award from the Alexander von Humboldt Foundation.

Funding for the Sloan Digital Sky Survey V has been provided by the Alfred P. Sloan Foundation, the Heising-Simons Foundation, the National Science Foundation, and the Participating Institutions. SDSS acknowledges support and resources from the Center for High-Performance Computing at the University of Utah. SDSS telescopes are located at Apache Point Observatory, funded by the Astrophysical Research Consortium and operated by New Mexico State University, and at Las Campanas Observatory, operated by the Carnegie Institution for Science. The SDSS web site is www.sdss.org.

This work has made use of data from the European Space Agency (ESA) mission *Gaia* (https://www.cosmos.esa.int/gaia), processed by the *Gaia* Data Processing and Analysis Consortium (DPAC, https://www.cosmos.esa.int/web/gaia/dpac/consortium). Funding for the DPAC has been provided by national institutions, in particular the institutions participating in the *Gaia* Multilateral Agreement.

This project has also benefited from using Claude Code for coding development and copy editing.



Facilities: Sloan (APOGEE), *Gaia*

Software: Astropy (Astropy Collaboration et al. 2013, 2018, 2022), NumPy (Harris et al. 2020), SciPy (Virtanen et al. 2020), Matplotlib (Hunter 2007), scikit-learn (Pedregosa et al. 2011), PyTorch (Paszke et al.

2019), LangGraph, the Model Context Protocol Python SDK, and the `gemini-2.5-flash` language model

REFERENCES

Ahumada R., et al., 2020, ApJS, 249, 3

Allende Prieto C., Beers T. C., Wilhelm R., Newberg H. J., Rockosi C. M., Yanny B., Lee Y. S., 2006, ApJ, 636, 804

Almeida A., et al., 2023, ApJS, 267, 44

Astropy Collaboration et al., 2013, A&A, 558, A33

Astropy Collaboration et al., 2018, AJ, 156, 123

Astropy Collaboration et al., 2022, ApJ, 935, 167

Badenes C., et al., 2018, ApJ, 854, 147

Belokurov V., et al., 2020, MNRAS, 496, 1922

Bergemann M., Lind K., Collet R., Magic Z., Asplund M., 2012, MNRAS, 427, 27

Blanco-Cuaresma S., Soubiran C., Heiter U., Jofré P., 2014, A&A, 569, A111

Bland-Hawthorn J., Gerhard O., 2016, ARA&A, 54, 529

Blanton M. R., et al., 2017, AJ, 154, 28

Boiko D. A., MacKnight R., Kline B., Gomes G., 2023, Nature, 624, 570

Bommasani R., et al., 2021, arXiv e-prints, p. arXiv:2108.07258

Bran A. M., Cox S., Schilter O., Baldassari C., White A. D., Schwaller P., 2023, arXiv e-prints, p. arXiv:2304.05376

Brown T. B., et al., 2020, arXiv e-prints, p. arXiv:2005.14165

Casey A. R., Hogg D. W., Ness M., Rix H.-W., Ho A. Q. Y., Gilmore G., 2016, arXiv e-prints, p. arXiv:1603.03040

Castelli F., Kurucz R. L., 2003, in Piskunov N., Weiss W. W., Gray D. F., eds, IAU Symposium Vol. 210, Modelling of Stellar Atmospheres. p. A20 (arXiv:astro-ph/0405087), doi:10.48550/arXiv.astro-ph/0405087

Choi J., Dotter A., Conroy C., Cantiello M., Paxton B., Johnson B. D., 2016, ApJ, 823, 102

Cui X.-Q., et al., 2012, Research in Astronomy and Astrophysics, 12, 1197

Daher C. M., et al., 2022, MNRAS, 512, 2051

Dotter A., 2016, ApJS, 222, 8

Duchêne G., Kraus A., 2013, ARA&A, 51, 269

El-Badry K., 2024, NewAR, 98, 101694

El-Badry K., Rix H.-W., 2018, MNRAS, 480, 4884

El-Badry K., Rix H.-W., Ting Y.-S., Weisz D. R., Bergemann M., Cargile P., Conroy C., Eilers A.-C., 2018a, MNRAS, 473, 5043

El-Badry K., et al., 2018b, MNRAS, 476, 528

El-Badry K., Rix H.-W., Tian H., Duchêne G., Moe M., 2019, MNRAS, 489, 5822

El-Badry K., Rix H.-W., Heintz T. M., 2021, MNRAS, 506, 2269

Fabbro S., Venn K. A., O'Briain T., Bialek S., Kielty C. L., Jahandar F., Monty S., 2018, MNRAS, 475, 2978

Fouesneau M., et al., 2024, arXiv e-prints, p. arXiv:2409.20252

Gaia Collaboration et al., 2016, A&A, 595, A1

Gaia Collaboration et al., 2023a, A&A, 674, A1

Gaia Collaboration et al., 2023b, A&A, 674, A34

García Pérez A. E., et al., 2016, AJ, 151, 144

Gunn J. E., et al., 2006, AJ, 131, 2332

Gustafsson B., Edvardsson B., Eriksson K., Jørgensen U. G., Nordlund Å., Plez B., 2008, A&A, 486, 951

Halbwachs J.-L., et al., 2023, A&A, 674, A9

Harris C. R., et al., 2020, Nature, 585, 357

Heiter U., Jofré P., Gustafsson B., Korn A. J., Soubiran C., Thévenin F., 2015, A&A, 582, A49

Hunter J. D., 2007, Computing in Science and Engineering, 9, 90

Hwang H.-C., Ting Y.-S., Zakamska N. L., 2022a, MNRAS, 512, 3383

Hwang H.-C., El-Badry K., Rix H.-W., Hamilton C., Ting Y.-S., Zakamska N. L., 2022b, ApJL, 933, L32

Jin S., et al., 2024, MNRAS, 530, 2688

Kervella P., Arenou F., Mignard F., Thévenin F., 2019, A&A, 623, A72

Kobulnicky H. A., Fryer C. L., 2007, ApJ, 670, 747

Kollmeier J. A., et al., 2017, arXiv e-prints, p. arXiv:1711.03234

Kounkel M., et al., 2021, AJ, 162, 184

Kraus A. L., Ireland M. J., Martinache F., Hillenbrand L. A., 2011, ApJ, 731, 8

Kroupa P., 1995, MNRAS, 277, 1491

Leung H. W., Bovy J., 2019, MNRAS, 483, 3255

Leung H. W., Bovy J., 2024, MNRAS, 527, 1494

Lindegren L., et al., 2021, A&A, 649, A2

Lu C., Lu C., Tjarko Lange R., Foerster J., Clune J., Ha D., 2024, arXiv e-prints, p. arXiv:2408.06292

Majewski S. R., et al., 2017, AJ, 154, 94

Mazzola C. N., et al., 2020, MNRAS, 499, 1607

Meibom S., Mathieu R. D., 2005, ApJ, 620, 970

Merle T., et al., 2017, A&A, 608, A95

Moe M., Di Stefano R., 2017, ApJS, 230, 15

Nakano R., et al., 2021, arXiv e-prints, p. arXiv:2112.09332

Ness M., Hogg D. W., Rix H.-W., Ho A. Y. Q., Zasowski G., 2015, ApJ, 808, 16
Nidever D. L., et al., 2015, AJ, 150, 173
Offner S. S. R., Moe M., Kratter K. M., Sadavoy S. I., Jensen E. L. N., Tobin J. J., 2023, in Inutsuka S., Aikawa Y., Muto T., Tomida K., Tamura M., eds, Astronomical Society of the Pacific Conference Series Vol. 534, Protostars and Planets VII. p. 275 (arXiv:2203.10066), doi:10.48550/arXiv.2203.10066
OpenAI et al., 2023, arXiv e-prints, p. arXiv:2303.08774
Ouyang L., et al., 2022, arXiv e-prints, p. arXiv:2203.02155
Paszke A., et al., 2019, arXiv e-prints, p. arXiv:1912.01703
Paxton B., Bildsten L., Dotter A., Herwig F., Lesaffre P., Timmes F., 2011, ApJS, 192, 3
Pedregosa F., et al., 2011, Journal of Machine Learning Research, 12, 2825
Penoyre Z., Belokurov V., Evans N. W., 2022, MNRAS, 513, 2437
Pourbaix D., et al., 2004, A&A, 424, 727
Price-Whelan A. M., Hogg D. W., Foreman-Mackey D., Rix H.-W., 2017, ApJ, 837, 20
Price-Whelan A. M., et al., 2018, AJ, 156, 18
Price-Whelan A. M., et al., 2020, ApJ, 895, 2
Raghavan D., et al., 2010, ApJS, 190, 1
Recio-Blanco A., Bijaoui A., de Laverny P., 2006, MNRAS, 370, 141
Recio-Blanco A., et al., 2023, A&A, 674, A29
Sana H., et al., 2012, Science, 337, 444
Schick T., Dwivedi-Yu J., Dessì R., Raileanu R., Lomeli M., Zettlemoyer L., Cancedda N., Scialom T., 2023, arXiv e-prints, p. arXiv:2302.04761
Seeburger R., Rix H.-W., El-Badry K., Xiang M., Fouesneau M., 2024, MNRAS, 530, 1935
Shahaf S., Bashi D., Mazeh T., Faigler S., Arenou F., El-Badry K., Rix H. W., 2023, MNRAS, 518, 2991
Steinmetz M., et al., 2006, AJ, 132, 1645
Ting Y.-S., Conroy C., Rix H.-W., Cargile P., 2019, ApJ, 879, 69
Ting Y.-S., Saad S. M., Liu F., Shen Y., 2026, The Open Journal of Astrophysics, 9, 1879
Tokovinin A., 2018, ApJS, 235, 6
Tokovinin A., Moe M., 2020, MNRAS, 491, 5158
Vaswani A., Shazeer N., Parmar N., Uszkoreit J., Jones L., Gomez A. N., Kaiser L., Polosukhin I., 2017, arXiv e-prints, p. arXiv:1706.03762
Virtanen P., et al., 2020, Nature Medicine, 17, 261
Wei J., et al., 2022, arXiv e-prints, p. arXiv:2201.11903
Wilson J. C., et al., 2019, PASP, 131, 055001
Wu Q., et al., 2023, arXiv e-prints, p. arXiv:2308.08155
Xiang M., et al., 2019, ApJS, 245, 34
Yao S., Zhao J., Yu D., Du N., Shafran I., Narasimhan K., Cao Y., 2022, arXiv e-prints, p. arXiv:2210.03629
Zucker S., Mazeh T., 1994, ApJ, 420, 806
de Haan T., et al., 2025, Scientific Reports, 15, 13751
de Jong R. S., et al., 2019, The Messenger, 175, 3

APPENDIX

A. THE JOINT KEPLERIAN SAMPLER

For system j with N_j visits we observe a primary and a secondary radial velocity at each epoch, together with the mass ratio q_j from the spectral decomposition (Section 4.4). The two stars share one Keplerian orbit, described by the period P, eccentricity e, argument of periastron ω, a reference phase ϕ, the primary velocity semi-amplitude K_1, and the systemic velocity $v_{\rm sys}$. We advance the mean anomaly linearly in time, solve Kepler's equation for the eccentric anomaly by Newton iteration, and convert to the true anomaly ν_i in the standard way. The two line-of-sight velocities then share one orbital shape g_i,

$$v^{\rm mod}_{{\rm rad},1,i} = v_{\rm sys} + K_1\, g_i, \qquad v^{\rm mod}_{{\rm rad},2,i} = v_{\rm sys} - \frac{K_1}{q}\, g_i, \qquad g_i \equiv \cos(\nu_i + \omega) + e\cos\omega, \tag{A1}$$

where the primary semi-amplitude $K_1 = 2\pi a_1 \sin i/(P\sqrt{1-e^2})$ absorbs the inclination, and the secondary amplitude is fixed to K_1/q by the spectroscopic mass ratio, so each epoch contributes two data points tied by one orbit. Radial velocities carry no plane-of-sky information, so the ascending node drops out, the inclination enters only through K_1, and the mass ratio $q = K_1/K_2$ stays free of it.

The nonlinear parameters carry wide priors, log-uniform in period from 0.5 to 5,000 days and uniform in e on $[0, 0.95]$ and in ϕ and ω. At fixed (P, e, ω, ϕ) the model of Equation (A1) is linear in $(K_1, v_{\rm sys})$, which we solve in closed form and marginalize as a Gaussian. The archive does not release a velocity uncertainty per visit, so one per-epoch dispersion s stands for all systems. Near $q = 1$ the decomposition can exchange the two components between visits, so we sum the likelihood over both assignments at each epoch, which marginalizes the labels at fixed orbit.

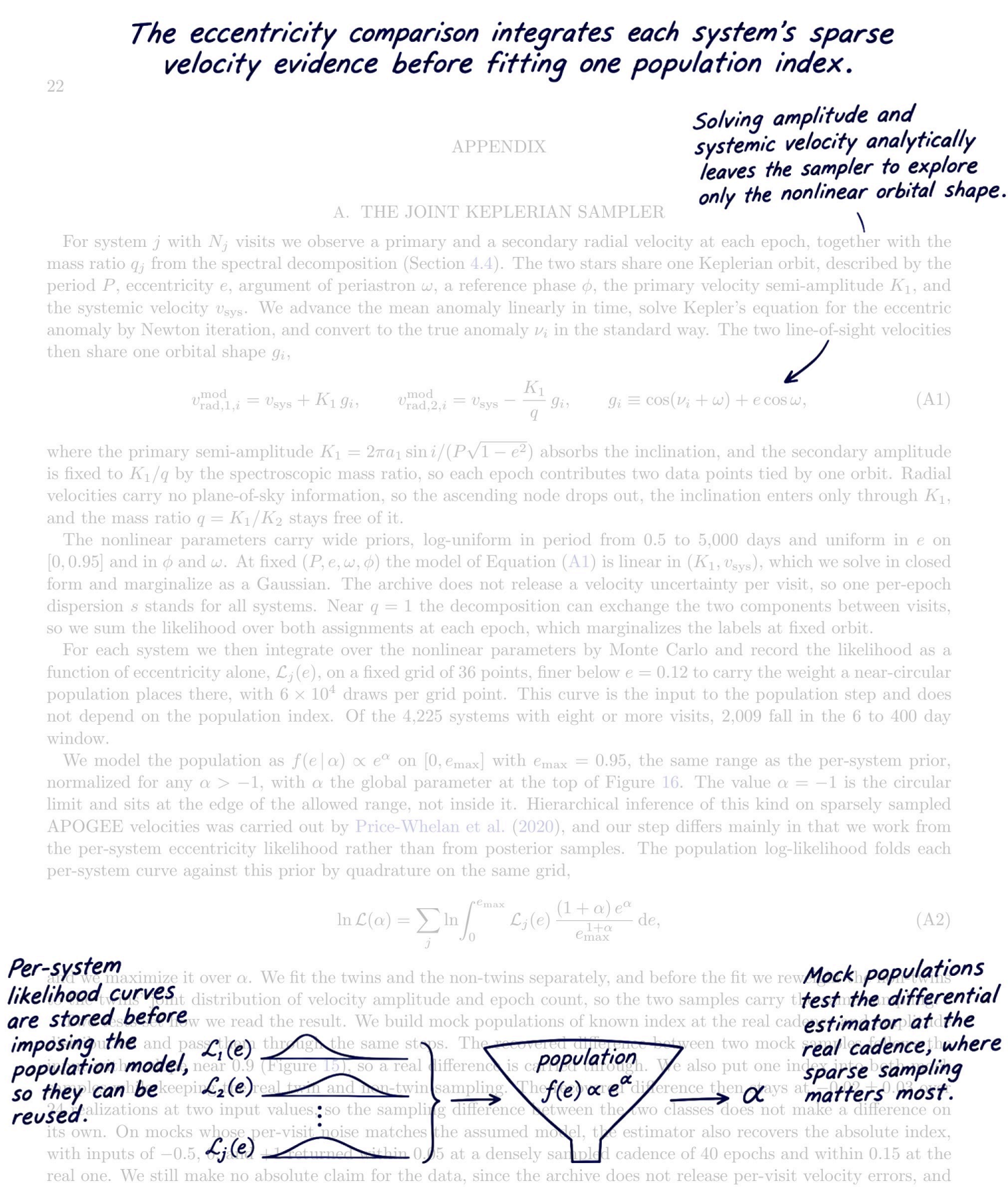
For each system we then integrate over the nonlinear parameters by Monte Carlo and record the likelihood as a function of eccentricity alone, $\mathcal{L}_j(e)$, on a fixed grid of 36 points, finer below $e = 0.12$ to carry the weight a near-circular population places there, with 6×10^4 draws per grid point. This curve is the input to the population step and does not depend on the population index. Of the 4,225 systems with eight or more visits, 2,009 fall in the 6 to 400 day window.

We model the population as $f(e\,|\,\alpha) \propto e^{\alpha}$ on $[0, e_{\rm max}]$ with $e_{\rm max} = 0.95$, the same range as the per-system prior, normalized for any $\alpha > -1$, with α the global parameter at the top of Figure 16. The value $\alpha = -1$ is the circular limit and sits at the edge of the allowed range, not inside it. Hierarchical inference of this kind on sparsely sampled APOGEE velocities was carried out by Price-Whelan et al. (2020), and our step differs mainly in that we work from the per-system eccentricity likelihood rather than from posterior samples. The population log-likelihood folds each per-system curve against this prior by quadrature on the same grid,

$$\ln \mathcal{L}(\alpha) = \sum_j \ln \int_0^{e_{\rm max}} \mathcal{L}_j(e)\, \frac{(1+\alpha)\, e^{\alpha}}{e_{\rm max}^{1+\alpha}}\, {\rm d}e, \tag{A2}$$

and we maximize it over α. We fit the twins and the non-twins separately, and before the fit we reweight the twins to the joint distribution of velocity amplitude and epoch count, so the two samples carry the same weight. Now we read the result. We build mock populations of known index at the real cadence and dispersion and pass them through the same steps. The recovered difference between two mock samples follows the input one-to-one near 0.9 (Figure 15), so a real difference is carried through. We also put one index into both samples, keeping the real twin and non-twin sampling. The recovered difference then stays at -0.02 ± 0.03 over the full range, with individual recoveries at two input values so the sampling difference between the two classes does not make a difference on its own. On mocks whose per-visit noise matches the assumed model, the estimator also recovers the absolute index, with inputs of -0.5, 0, and $+1$ returned within 0.05 at a densely sampled cadence of 40 epochs and within 0.15 at the real one. We still make no absolute claim for the data, since the archive does not release per-visit velocity errors, and a misstated dispersion moves the absolute index of both samples together, which is what the differential removes.

Three twin-specific effects sit outside these tests, and we note the direction of each. The label ambiguity and the line blending near conjunction act on near-equal pairs alone and push $\alpha_{\rm twin}$ down, in the direction of the measured difference. The mass ratio is held at its spectroscopic value, which is least certain near $q = 1$. Contamination runs



The hierarchical model ties all visits within each binary and all binaries through the shared eccentricity distribution.

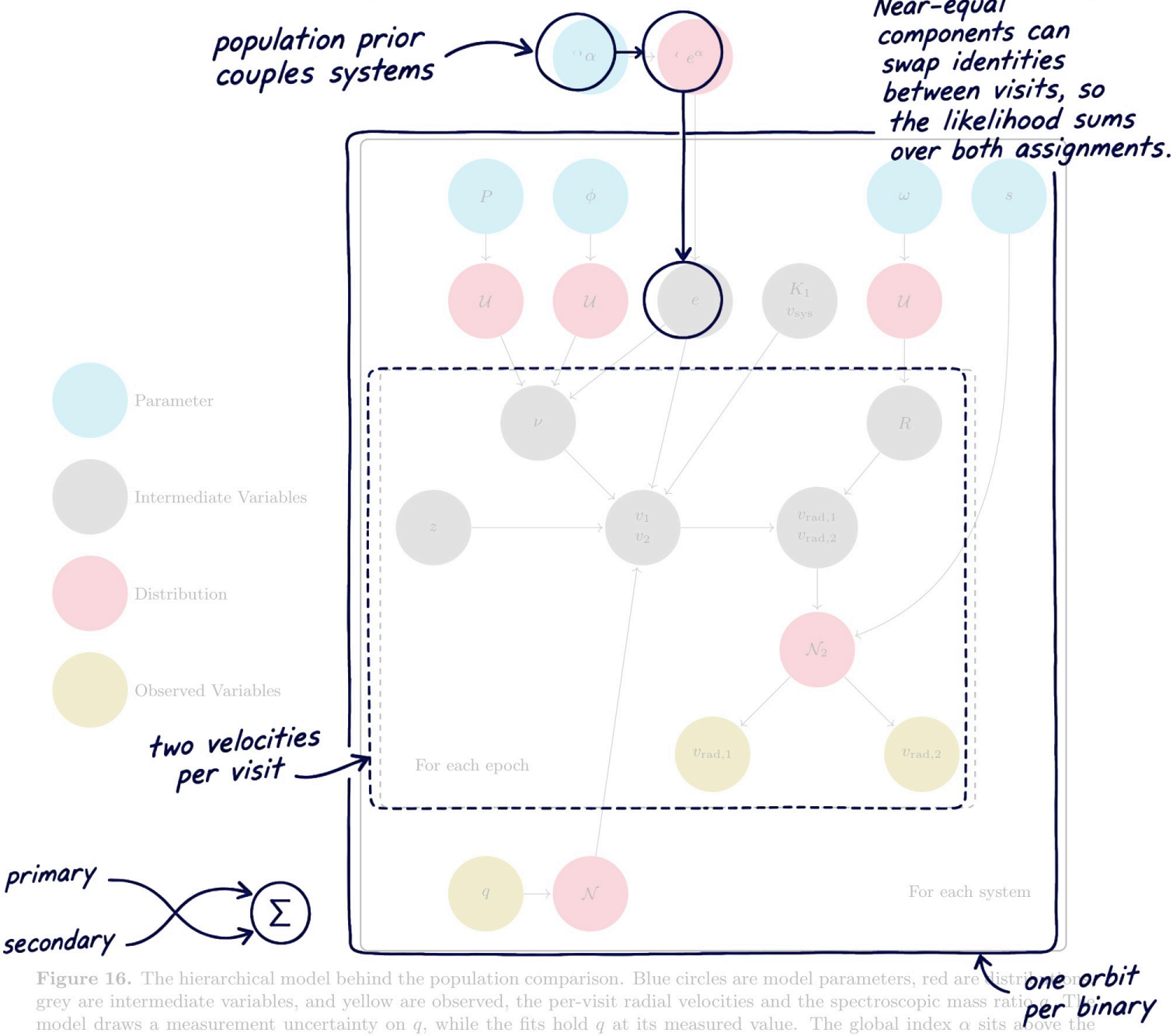


Figure 16. The hierarchical model behind the population comparison. Blue circles are model parameters, red are distributions, grey are intermediate variables, and yellow are observed, the per-visit radial velocities and the spectroscopic mass ratio. The model draws a measurement uncertainty on q, while the fits hold q at its measured value. The global index α sits above the per-system plate and ties the eccentricities together through the population prior $f(e) \propto e^{\alpha}$, estimated from the per-system eccentricity likelihoods.

the other way, since the twins carry slightly more of it and noisy velocities read as eccentric, which would raise α_{twin}. None of these cancels in the differential, which is one reason we report a bound rather than a difference.

Twin-specific blending and label ambiguity do not cancel perfectly; that is why we report a bound.